





The Wind Temperature and Mass-loss Rate of Arcturus (K1.5 III)

Graham M. Harper¹ , Thomas R. Ayres¹ , and Eamon O’Gorman²¹ Center for Astrophysics and Space Astronomy, University of Colorado Boulder, Boulder, CO 80309, USA; graham.harper@colorado.edu² Astronomy & Astrophysics Section, Dublin Institute for Advanced Studies, Center for Astrophysics and Space Astronomy, Dublin 6 D04 XF86, Ireland

Received 2022 January 27; revised 2022 April 19; accepted 2022 April 21; published 2022 June 15

Abstract

In this paper we aim to constrain the wind temperature, outflow and turbulent velocities, ionization state, and mass-loss rate of the single red giant Arcturus (α Boo K1.5 III) using high spectral resolution Hubble Space Telescope Space Telescope Imaging Spectrograph profiles of Si III 1206.5 Å, O I 1304 Å and 1306 Å, C II 1334 Å and 1335 Å, and Mg II h 2802 Å. The use of the E140-H setting for α Boo allows the Si III 1206.5 Å line to be cleanly extracted from the echelle format for the first time. The ratios of the wind optical depths of lines from different species constrain the temperature at the base of the wind to $T_{\text{wind}} \sim 15,400$ K. The mass-loss rate derived is $2.5 \times 10^{-11} M_{\odot} \text{ yr}^{-1}$ for Epoch 2018–2019, smaller than previous semiempirical estimates. These results can be reconciled with multiwavelength Very Large Array radio continuum fluxes for Epoch 2011–2012 by increasing the temperature to $T_{\text{wind}} \sim 18,000$ K, or increasing the mass-loss rate to $4.0 \times 10^{-11} M_{\odot} \text{ yr}^{-1}$. Interpreting the wind acceleration and turbulence in terms of a steady WKB Alfvén wave-driven wind reveals that the wave energy damping length increases with increasing radius, opposite to the trend expected for ion-neutral damping of monochromatic waves, confirming a previous result by Kuin and Ahmad derived for ζ Aur binaries. This implies that a spectrum of waves is required in this framework with wave periods in the range of hours to days, consistent with the photospheric granulation timescale. Constraints on a radial magnetic field (B) at $1.2 R_*$ are an upper limit of $B \leq 2$ G from the implied wave heating, and $B \geq 0.3$ G to avoid excessive wave amplitudes.

Unified Astronomy Thesaurus concepts: [Stellar winds \(1636\)](#); [Alfvén waves \(23\)](#); [Stellar spectral lines \(1630\)](#); [Hubble Space Telescope \(761\)](#); [Stellar mass loss \(1613\)](#)

Supporting material: figure set

1. Introduction

Understanding the processes that drive mass loss from noncoronal nonpulsating K through mid-M red giants is one of the major unsolved challenges in stellar astrophysics. From a physics standpoint, the interaction of magnetic waves and partially ionized plasma is of wide importance, and from an astrophysics standpoint, quantifying mass loss is crucial for stellar evolution codes that are used to help understand chemical galactic evolution. While significant progress has recently been made in understanding the winds from asymptotic giant branch stars, driven by pulsational levitation and radiation pressure on dust (Höfner & Olofsson 2018), for K through mid-M red giants and supergiants, there remains a significant gulf between observations and theoretical models.

Deutsch (1956) first demonstrated direct proof of mass loss from α^1 Her (M5 II), but in the intervening half century, the details of the physical processes that drive stellar outflows (also called winds) from nonpulsating cool evolved stars have remained elusive. Worse, there are few well-established mass-loss rates. The earliest measures of gas lost from K and M red giants and supergiants were based on optical diagnostics. Unfortunately most of these lines are from minority species (Sanner 1976; Bernat 1977; Hagen 1978), or from excited states, which makes them sensitive to uncertainties in the line formation, e.g., H α (Mallik 1982; Mallik 1993, and references therein) and He I 10830 Å (Sasselov & Lester 1994). It is now

known that calcium is photoionized to Ca III by the chromospheric radiation fields in K and early-M evolved stars, making mass-loss rate estimates based on the well-observed Ca II H & K lines less reliable (e.g., Wilson 1960). A summary of early optical studies of mass loss has been given by Reimers (1975a).

Studies of wide binary systems containing a cool evolved star, albeit limited in number, have provided robust estimates of stellar mass-loss rates. In these systems, the position of the companion constrains the radial distance associated with inferred line-of-sight column densities derived from line profiles or curve-of-growth analyses (Reimers 1975b; Kudritzki & Reimers 1978). These systems have been used to calibrate the empirical mass-loss formula

$$\dot{M} (M_{\odot} \text{ yr}^{-1}) = \eta \times 4 \times 10^{-13} \left(\frac{L_*}{L_{\odot}} \right) \left(\frac{g_{\odot}}{g_*} \right) \left(\frac{R_{\odot}}{R_*} \right) \quad (1)$$

where the original value of $\eta = 1.0$ (Reimers 1975a) was later revised to $\eta = 1.4$, with other studies of nonbinary samples finding different values for η (see Kudritzki & Reimers 1978, and references therein). Schröder & Cuntz (2005) presented a modified form of Equation (1) to include a term for the spatial extent of the atmosphere.

For such stellar parameter mass-loss rate scalings to be useful for stellar evolution codes, they must reflect the physical processes that drive the outflows so that they can be applied to broad regions of the Hertzsprung–Russell Diagram (HRD). Correlation of cool evolved star mass-loss rates with stellar properties have not yet proven to be insightful. This may be because “An important property of cool evolved stars is that they exist on branches in parameter space, on which



Original content from this work may be used under the terms of the [Creative Commons Attribution 4.0 licence](#). Any further distribution of this work must maintain attribution to the author(s) and the title of the work, journal citation and DOI.

fundamental parameters (T_{eff} , $\log g$, pulsational properties ...) are themselves correlated” (Judge 1992). Clearly understanding the wind acceleration and, if possible, the wind temperature are also requisite to understanding the physics of mass loss.

With near-ultraviolet (NUV) spectra from International Ultraviolet Explorer (IUE) and Hubble Space Telescope (HST), line diagnostics with a large range of opacities from dominant ionization stages became available. Some of the best determined wind acceleration and mass-loss rates for intermediate-mass, $2\text{--}8 M_{\odot}$ evolved stars are from the eccentric ζ Aur eclipsing binary systems (Reimers 1987; see their Figure 10), which suggests a reduction of η to ~ 0.4 for these stars. NUV and far-UV (FUV) spectra have also enabled wind analyses of evolved single stars: α Boo (K1.5 III; Drake 1985), α TrA (K2 III; Harper et al. 1995), α Tau (K5 III) and γ Dra (K5 III; Robinson et al. 1998), λ Vel (K4 Ib; Carpenter et al. 1999), and μ Gem (M3 IIIab) and γ Cru (M3.4 III; Rau et al. 2018). A key result from all of these studies is that the winds appear to continue to accelerate outwards, and they are not a result of ballistic ejections from the surface.

It is not clear from these latter studies how accurate Equation (1) is for mass-loss rates for low-mass, $<2 M_{\odot}$ red giants. For example, Equation (1) with the stellar parameters of α Boo from Maeckle et al. (1975) and $\eta = 0.4$ for metal-poor stars (Renzini 1977), gives a mass-loss rate of $7 \times 10^{-10} M_{\odot} \text{ yr}^{-1}$, which is greater than $2 \times 10^{-10} M_{\odot} \text{ yr}^{-1}$ found by Drake (1985). The discrepancy for α Tau (K5 III) is worse with Robinson et al. (1998) finding $\dot{M} \simeq 1.4 \times 10^{-11} M_{\odot} \text{ yr}^{-1}$, compared to $8 \times 10^{-9} M_{\odot} \text{ yr}^{-1}$ with $\eta = 1.4$. The classic Reimers’ formula overpredicts mass-loss rates for all of these lower-mass single red giants. Furthermore, it is not known how binarity affects the mass-loss process, and whether or not the acceleration from these systems is characteristic of single stars. For example, the wind acceleration of ζ Auriage A (K4 Ib) and the spectral-type proxy λ Vel (K4 Ib) appear quite different. The former has a slow acceleration (Baade et al. 1996; Harper et al. 2005) while the latter has a more rapid acceleration close to the star (Carpenter et al. 1999), typical of lower-mass single red giant stars.

In this paper we present a detailed analysis of the wind of the mildly metal-poor Arcturus (α Boo K1.5 III; HD 124897, HR 5340), and compare the results to other red giant studies. These stars lie in the region of the HRD where there is a low level of optical variability (Henry et al. 2000), and show little or no circumstellar wind dust (Zuckerman et al. 1995); they also do not show the presence of molecules, namely CO. The low amplitude optical variability and absence of significant photospheric radial velocity variation rule out pulsation-driven mass loss, and the lack of molecules or dust rules out a radiation pressure source. Acoustic shock waves damp too close to the star, but potentially heat the chromosphere (Cuntz 1990), and the absence of significant coronal plasma (Linsky & Haisch 1979; Haisch et al. 1991) rules out high-temperature Parker-type thermal winds. For a review of physical considerations related to general mass-loss processes, see Holzer & MacGregor (1985).

The mass-loss mechanism is thought instead to be related to some form of magnetic wave process ultimately driven by convective motions in or below the photosphere (Lamers & Cassinelli 1999). Photospheric magnetic fields have now been detected on many K and M giants (Aurière et al. 2015, and

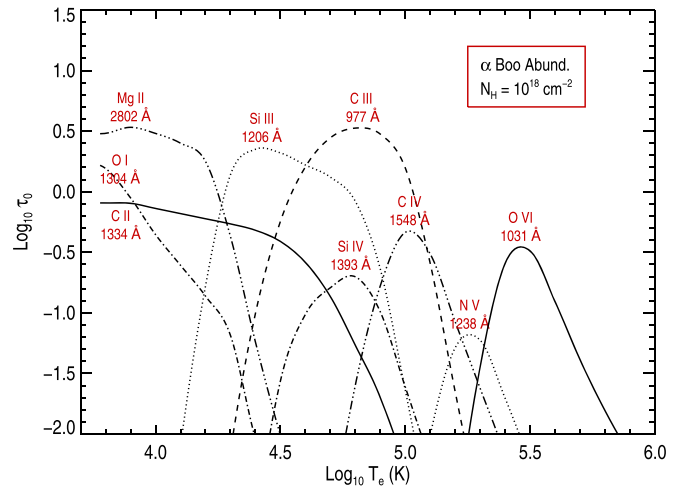


Figure 1. Line center optical depths for potential diagnostic wind scattering lines vs. constant wind electron temperature, T_e . The optical depths assume a hydrogen column density of $N_{\text{H}} = 10^{18} \text{ cm}^{-2}$, abundances from Table 1, and a combination of static chromospheric and coronal approximation ionization balances. The assumed wind turbulence is assumed to scale with the hydrogen sound speed. While the O I, C II, and Mg II lines become less opaque with increasing constant wind temperature, the Si III 1206.5 Å line becomes much more opaque between $\text{Log}_{10} T_e = 4.1$ and 4.4. The comparison of the actual optical depth in all of these lines provides a tight constraint on the wind temperature.

references therein), and mean longitudinal magnetic fields of ~ 0.4 G have been detected on α Boo (Sennhauser & Berdyugina 2011; Aurière et al. 2015). α Boo shows activity-related chromospheric variations (Brown et al. 2008), and is a weak X-ray source (Ayres et al. 2003; Ayres 2018), both suggesting that magnetic fields play an important role in the structure and energy balance of the extended atmosphere.

To drive a stellar wind, the outward propagating wave energy (of any kind) must not dissipate too rapidly. Incompressible Alfvén waves can, in principle, satisfy this requirement. Hartmann & MacGregor (1980) examined 1D Wentzel–Kramers–Brillouin (WKB) Alfvén wave–driven wind models and found that a damping length of the order of the stellar radius is required to ensure that the terminal (asymptotic) winds speeds, V_{∞} , are not too high. For K and M giants, V_{∞} is a fraction, $\sim 1/3$, of the surface escape speed, $V_{\text{esc}}(R_*)$, and wind radiative losses are small, so that most of the wave energy, $\propto V_{\text{esc}}^2$ goes into overcoming the gravitational potential (see Judge & Stencel 1991). The fine-tuning of the damping of waves to drive massive outflows with low asymptotic speeds has been discussed by Holzer et al. (1983). One consequence of the required wave damping is that the wind should be heated to chromospheric temperatures or higher, and the models of 1980’s era predicted significant UV emission. With the advent of high signal-to-noise ratio (S/N) and high spectral resolution HST spectra, it became apparent that the observed emission line profiles did not reflect a stellar outflow (Harper 2001); i.e., optically thin emission lines from different excitation energies do not show outflow-induced blueshifts. To find the expected radiative loss channels from stellar outflows, the wind temperature needs to be determined. This is a principal limitation of previous single star studies—they do not provide strong constraints on the wind temperatures.

Figure 1 shows the optical depths of different UV emission lines computed under the assumption of a wind with a constant

Table 1
Stellar Properties of Arcturus

Property	Value	Reference/Note
HD	124897	
HR	5340	
MK Spectral-Type	K1.5 III	Keenan & McNeil (1989)
B-V	1.23	
Angular Diameter (mas)	21.05 ± 0.21	Lacour et al. (2008), see also Heiter et al. (2015)
Parallax (mas)	88.83 ± 0.54	van Leeuwen et al. (2007)
Distance (pc)	11.26 ± 0.07	From Parallax
Radius (R_{\odot})	25.4 ± 0.2	From Angular Diameter and Distance
T_{eff} (K)	4286 ± 35	Heiter et al. (2015)
$L(L_{\odot})$	170	
$\text{Log } g_{*}$ (cm s^{-2})	1.6 ± 0.2	Heiter et al. (2015)
$v_{\text{esc}}(R_{*})$ (km s^{-1})	124	Surface escape speed from Mass and Radius
v_{chrom} (km s^{-1})	$\simeq 14$	isotropic/most prob. vel. C II] 2325 Å Mult.
v_{wind} (km s^{-1})	40–50	Ayres et al. (1982); McClintock et al. (1978)
$v \sin i$ (km s^{-1})	2.4 ± 1.0	Carney et al. (2008)
v_{macro} (km s^{-1})	5.2 ± 1.0	Radial-Tangential: Carney et al. (2008)
Radial Velocity (km s^{-1})	–5.2	See text
[Fe/H]	-0.52 ± 0.04	Jofré et al. (2014)
$A(\text{He})$	8.3×10^{-2}	Adopted by Drake (1985)
$A(\text{Mg})$	$3.1 (\pm 0.9) \times 10^{-5}$	Jofré et al. (2015)
$A(\text{Si})$	$1.7 (\pm 0.4) \times 10^{-5}$	Jofré et al. (2015)
$A(\text{C})$	$1.2 (\pm 0.5) \times 10^{-4}$	Ryde et al. (2010)
$A(\text{O})$	$5.0 (\pm 1.5) \times 10^{-4}$	Ryde et al. (2010)
$A(\text{Fe})$	$8.5 (\pm 1.6) \times 10^{-6}$	Jofré et al. (2015)
Mass (M_{\odot})	1.0 ± 0.2	Heiter et al. (2015)

Note. Gaia FGK benchmark reference star (Heiter et al. 2015).

velocity, a hydrogen column density of $N_{\text{H}} = 10^{18} \text{ cm}^{-2}$; abundances are from Table 1, at different fixed, i.e., isothermal, temperatures (T_e). The microturbulence is assumed to scale with the sound speed, namely $\propto \sqrt{T_e}$. The ionization balances here are assumed static (Arnaud & Rothenflug 1985), modified for chromospheric photoionization of low first ionization potential elements. The relative optical depths give an indication of which diagnostic lines will be useful in different temperature regimes. Above 10^4 K , the optical depth of Si III 1206.5 Å increases strongly with increasing temperature, and might induce a wind-scattered profile asymmetry. Therefore a comparison of the Si III 1206.5 Å profile with those from the resonance lines of O I, C II, and Mg II, which become less opaque with increasing temperature, because they start to ionize to the next ionization state, can constrain the wind temperature. Unfortunately obtaining a Si III 1206.5 Å line profile with the sensitive HST-STIS E140M is difficult because of the relative position of the line to H I Ly α on the echellegrams, but here we present the first HST–Space Telescope Imaging Spectrograph (STIS) spectra of α Boo that overcome previous technical challenges.

The structure of this paper is as follows: The new HST-STIS observations are described in Section 2, and a detailed description of the methods adopted to characterize α Boo’s wind are given in Section 3. The results of the wind scattering line profile calculations are presented in Section 4, and the

interpretation is discussed in Section 5. The semiempirical interpretation of the wind acceleration and turbulence in the framework of Alfvén wave–driven winds is presented in Section 6. Our discussion and conclusions are presented in Sections 7 and 8, respectively.

2. HST-STIS Observations

Arcturus was previously recorded in the FUV by STIS on only one occasion, in 1998 August, early in the STIS operations. The observation was with the medium-resolution echelle grating, E140M-1425, which covers the range 1150–1720 Å. The default narrow spectroscopic slit, $0.2'' \times 0.06''$, was used, delivering the maximum spectral resolution, $R = \lambda/\Delta\lambda_{\text{FWHM}} = 45,000$. The exposure time was 5.2 ks. The narrow slit, however, reduced the FUV throughput significantly, impacting the S/N. Further, the choice of the medium-resolution echelle, although achieving the maximum spectral coverage for the exploratory program, had the unintended consequence that severe cross-dispersion scattered light from extremely bright chromospheric H I 1215 Å Ly α washed over adjacent echelle orders, essentially obliterating key species near Ly α , especially the crucial wind diagnostic, Si III 1206 Å. The initial STIS FUV spectrum of Arcturus was described by Ayres et al. (2003).

The new program on Arcturus largely was motivated by the desire to recover the pivotal Si III 1206 Å resonance line, to address questions concerning the strength and physical nature of the mass outflow of the archetypal red giant. To accomplish the separation of Si III from Ly α , the STIS high-resolution echelle, E140H, was utilized. The higher dispersion of the grating spreads out the Ly α scattered light, so that it is less impactful for the neighboring echelle orders; the Si III feature in E140H falls two echelle orders below Ly α , rather than in the next order down in E140M; and—most important—Si III in E140H is shifted in the 2D echelle format horizontally relative to Ly α , so that it misses the major swath of the vertically cross-dispersed scattered light. A comparison between the two types of echellegrams will be provided shortly.

The new program utilized the 1271 Å CENWAVE (which covers 1163–1356 Å) and the 1307 Å CENWAVE (1199–1397 Å). Both of these settings record the desired Si III feature, but on different parts of the FUV MAMA camera, so the combination of the two can partially mitigate detector fixed pattern noise. Further, 1271 + 1307 covers the widest range of accessible wavelengths (the STIS sensitivity falls rapidly below 1150 Å) of any of the pairs of neighboring E140H settings that also include Si III, thus enhancing the range of additional potential diagnostics.

The new program was scheduled for a four-orbit visit on 2018 June 26. The first two orbits were dedicated to CENWAVE 1271 and the subsequent two orbits to 1307. Following the guide star (GS) acquisition, Arcturus was initially captured using a brief exposure by the CCD camera with the F25ND5 filter. The target centering was further refined by a dispersed-light peak-up with the CCD moderate-resolution first-order grating G430M-3680 and the ND2-filtered 0.2X0.05ND slit. The remainder of the first orbit was taken up by the first of the two E140H-1271 exposures. The aperture selected for the observation was the $0.2'' \times 0.2''$ “photometric” slot, which provides maximum throughput, although reducing the native 114,000 resolution of E140H somewhat (not a concern for the program, because the stellar lines, especially

Table 2
FUV Observations of α Boo

Dataset	UT Start (YYYY-MM-DD.dd)	$T(\text{exp})$ (s)	Aperture ($'' \times ''$)	Grating-CENWAVE (\AA)
Program 7733				
O4Y701030	1998-08-24.85	5208	0.2×0.06	E140M-1425
Program 15234				
ODIK01010	2018-06-26.52	1656	0.2×0.2	E140H-1271
ODIK01020	2018-06-26.57	2964	0.2×0.2	E140H-1271
ODIK01030	2018-06-26.64	0	0.2×0.2	E140H-1307
ODIK01040	2018-06-26.70	0	0.2×0.2	E140H-1307
ODIK51010	2019-07-07.80	2137	0.2×0.2	E140H-1307
ODIK51020	2019-07-07.86	2277	0.2×0.2	E140H-1307

Si III, are broad and fully resolved). A nonstandard, 50 s wavelength calibration exposure (several times deeper than the default) was paired with the first E140H setting to ensure an accurate wavelength scale zero-point, given that the hollow-cathode calibration lamp had faded over time, especially in the FUV.

A second E140H-1271 was slated for the second orbit, with a longer exposure than in the first, given that the somewhat time-consuming initial GS and target acquisitions, and peak-up, had already been done, and only a GS reacquisition was needed at the beginning of the orbit. Again, nonstandard WAVE exposures were taken. Both of the E140H-1271 observations were successful.

The third and fourth orbits of the visit were intended to collect the remaining two E140H-1307 exposures. Unfortunately, the GS reacquisition at the beginning of the third orbit failed, the STIS shutter remained closed for the rest of the visit, and no useful data were returned.

The two E140H-1307 exposures were rescheduled for about 1 yr later, on 2019 July 7, in a two-orbit repeat visit. These exposures, including the associated nonstandard WAVEs, were successful. All of the FUV exposures of Arcturus are summarized in Table 2. The total exposures in the new program were 4.6 ks in CENWAVE 1271 and 4.4 ks in 1307.

Figure 2 compares the earlier E140M-1425 echellegram of Arcturus to the more recent E140H-1271 exposures. The raw images (coadds of two subexposures for 1425, and the two separate exposures for 1271) are presented with the same intensity stretch, and in reverse gray scale. Also illustrated are the equivalent spectral ranges from the same FUV medium-resolution and high-resolution CENWAVEs of another nearby red giant, β Geminorum (HD 62509; K0 III; $d = 10.4$ pc). Unlike Arcturus, β Gem shows no evidence for a cool chromospheric wind.

The $\text{Ly}\alpha$ emission of β Gem is much reduced, and the key Si III 1206 \AA feature is unaffected by scattered light in the E140M raw image. (The β Gem images are coadditions over several independent echellegrams, including subexposures, from the Advanced Spectral Library Project ASTRAL³.)

2.1. Data Analysis

The STIS high-resolution echellegrams of Arcturus were processed through the CALSTIS⁴ pipeline, yielding the

standard high-level “x1d” files. These are tabulations of the spectral parameters—wavelengths, fluxes, and photometric errors—separately for the several dozen individual echelle orders. The extracted spectra were corrected by the pipeline for wavelength zero-point shifts deduced from the accompanying WAVE exposures.

The post-processing involved several steps. First, the individual spectral orders in the x1d file were merged, weighted according to the echelle sensitivity curves in the overlap regions. Second, the two E140H-1271 and two E140H-1307 exposures were separately coadded, registering the velocity scale of the second exposure of each pair to that of the first by cross-correlation of a reference emission feature. The exposure of a sequence closest to the centering peak-up (here, the first in each separate visit) likely has the most reliable absolute wavelength scale. Subsequent exposures might experience small shifts due to drifts of the stellar image in the aperture.) The velocity cross-correlation reference feature was chosen to be a bright, narrow emission within the CENWAVE 1271–1307 overlap region, in this case the Si I 1295 \AA line (which is radiatively fluoresced by the atomic oxygen triplet near 1305 \AA). The result of the second step was a coadded spectrum for the pair of 1271 exposures, and a corresponding one for the 1307 pair. These two coadded spectra then were spliced together over the wavelengths in common, again registering the velocity scales by cross-correlating the same Si I feature, to produce a final spectrum covering the full wavelength range, with an enhanced S/N in the (considerable) overlap zone, especially at Si III 1206 \AA . The various internal velocity cross-correlation corrections typically were small, <0.5 km s⁻¹, thanks to the special wavecal exposures.

Figure 3 compares the extracted spectra from the earlier E140M observation of Arcturus with that of the new merged, coadded, and spliced E140H echellegrams, smoothed by an FWHM = 6 pixel Gaussian to mimic the reduced resolution of the former. Several wavelength segments are shown: the vicinity of $\text{Ly}\alpha$, encompassing the Si III feature of interest, and for additional important wind lines including the O I triplet near 1305 \AA , and the C II multiplet near 1335 \AA . Also included is a similar comparison with the β Gem E140M and E140H-1271 coadded spectra.

2.2. Supplementary HST-STIS Data Sets

In addition to the FUV data sets, we also consider the NUV data sets given in Table 3 from StarCAT (Ayres 2010).

³ <https://casa.colorado.edu/ayres/ASTRAL>

⁴ <https://hst-docs.stsci.edu/stisdhb/chapter-3-stis-calibration/3-1-pipeline-processing-overview>

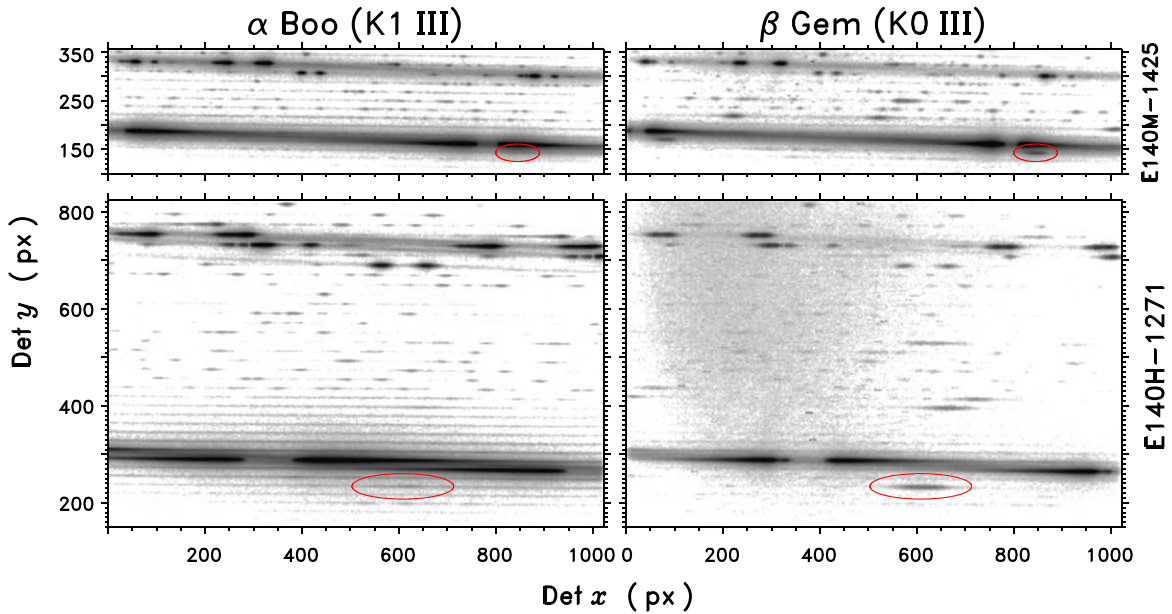


Figure 2. STIS raw echellegrams, medium-resolution E140M-1425 (upper) and high-resolution E140H-1271 (lower), for the red giants α Boo (left) and β Gem (right). The x - and y -axes are pixel coordinates in the 1024×1024 image format. Both the E140M and E140H segments cover about the same wavelength span in the y -direction: the former is more compact owing to the $2.5\times$ lower dispersion. The images are in counts per second with a logarithmic stretch between 10^{-4} and 0.1 cnt s^{-1} in reverse gray scale. The β Gem count rates were multiplied by three to compensate for the 1.2 mag difference in the visual (V) magnitudes. The raw images are coadditions over subexposures, if any, and over separate exposures within the same visit (α Boo) or several different visits (β Gem). The total exposures for β Gem were 19.1 ks for 1425, and 14.3 ks for 1271. For α Boo, the corresponding exposures were 5.2 ks and 4.6 ks. The location of the key Si III 1206 Å resonance line is circled in each image. Although Si III is clearly seen in β Gem just below H I 1215 Å Ly α in the E140M frame, the (weaker) counterpart in α Boo is lost in the scattered light glare from the broader Ly α emission. (Note that Si III also appears on the left-hand side of the E140M segment, in the overlapping echelle order one above.) In E140H, on the other hand, Si III not only falls two orders down from Ly α , but also is located below the less-intense wings of the hydrogen emission, instead of just under the bright red peak as in E140M. This separation allows the faint Si III emission in Arcturus to be extracted without interference from Ly α scattered light.

3. Characterizing the Wind Properties

To characterize α Boo’s wind properties, we model the wind scattering of photons in FUV and NUV emission lines from dominant ionization stages of abundant species. In an outflow, the photons, which are scattered from the blue part of the emission profile, are re-emitted toward longer wavelengths, and the degree of induced asymmetry is related to the number of scattering atoms and ions and hence the mass-loss rate. The best diagnostics are emission lines whose widths are in excess of the terminal wind speed, so that the scattering lies within the emission profile. We adopt the approach that the complex and dominant photon creation region (the chromosphere/transition region; see, for example, Ayres et al. 2003) is physically separated from the wind scattering region, and we model the scattering region only. This is justified by the absence of notable blueshifted emission from low optical depth chromospheric emission lines such that one would expect if this emission was created within the wind near the star. Consequently, the outward propagating radiation in the spectral line must be specified at the base of the outflow. In practice, in the absence of additional detailed empirical information, the specific intensity at the wind boundary condition is assumed to be independent of angle, i.e., isotropic—as adopted in previous similar studies (Harper et al. 1995; Robinson et al. 1998; Carpenter et al. 1999; Rau et al. 2018). For a discussion of the adopted input profiles, see Section 3.3.3. We note that the quite Sun center-to-limb Mg II h & k line Interface Region Imaging Spectrometer profiles reveal a center-to-limb flux ratio of ~ 1.5 (neglecting off-limb emission), or 20% about a mean value (Gunár et al. 2021).

The spherical moving atmosphere radiation transfer problem was solved using a variant of the S-MULTI code (Harper 1994), in which the formal solutions are made in the *Observer’s Frame* while *complete frequency redistribution* of the scattered photons was evaluated in the frame of the wind. The wind-induced Doppler shifts dominate the photon frequency redistribution, and *partial frequency redistribution* is not important within the wind (Drake & Linsky 1983). Each transition is treated as an equivalent two-level atom (ETLA). The ratio of the terminal speed to the turbulence at the wind base boundary condition (BC) is $V_\infty/V_{\text{turb}} \sim 2$ (based on the observed terminal wind speed, and the values for turbulence we find in Section 4) and eventually increasing outwards. The commonly assumed, and further simplified radiative transfer problem, large velocity gradient approximation with the Sobolev with exact integration (SEI) approach would be physically less accurate. The SEI approach assumes that a radiative transition’s mean intensity, and hence source function, at one radius is decoupled from that at adjacent radii, which is not accurate when the line is optically thick and $V_\infty/V_{\text{turb}} < 5$ (Schoenberg 1985). In practice, when nonlocal line scattering influences the source function, the SEI approach is no longer accurate (see Appendix A of Carpenter et al. 1999, for some comparative computations).

3.1. Diagnostics and Atomic Data

The emission line profiles modeled, and presented here are Si III 1206.5 Å, O I 1304 Å, O I 1306 Å, C II 1334 Å, C II 1335 Å, and Mg II h 2802 Å, while other emission lines from Fe II and Si II were found not to be useful. The Fe II and Si II

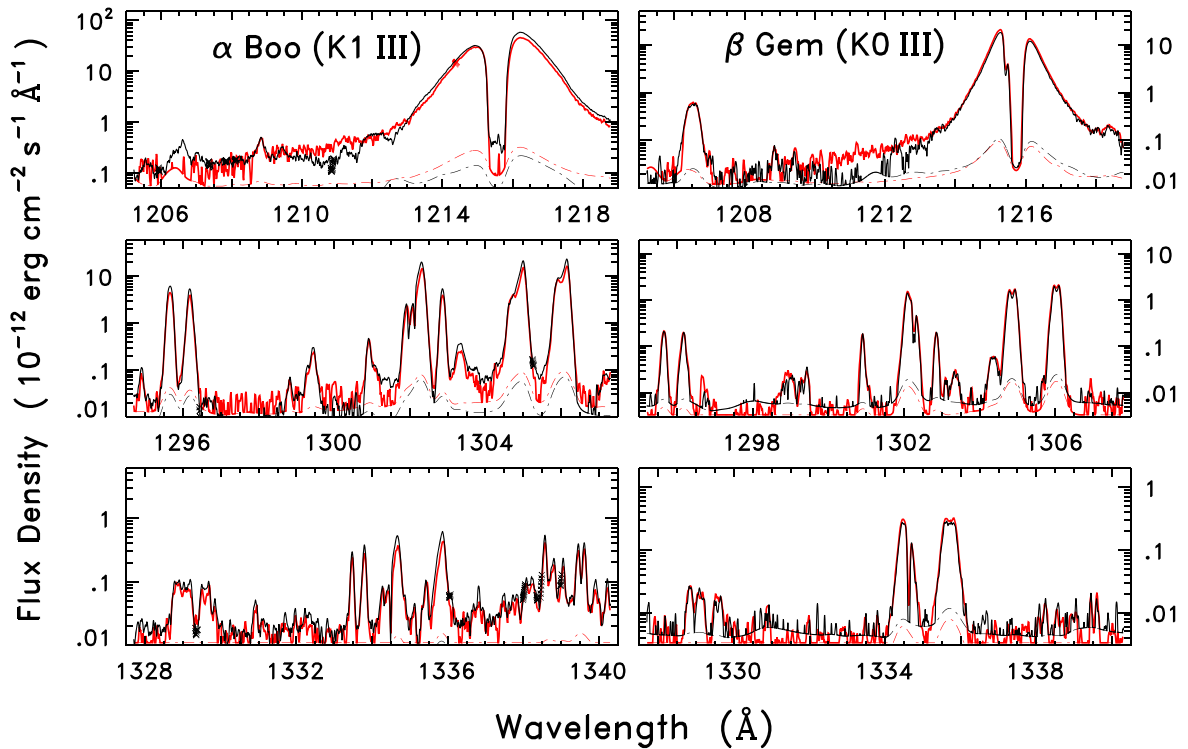


Figure 3. Spectral tracings from E140M (red solid) and E140H (dark solid), for the two red giants. The 1σ photometric errors, per 2-pixel resolution element (resel), are the red and dark dotted–dashed curves, for E140M and E140H, respectively. Small “x” symbols, with same color-coding, mark pixels that were flagged in the pipeline processing (for potential defects). The medium-resolution spectra were smoothed with a 2-pixel FWHM Gaussian, while the high-resolution tracings were smoothed with a 5-pixel FWHM Gaussian, to roughly achieve similar resolution. The Si III 1206.5 Å feature in β Gem is prominent, similar in strength to the C II multiplet near 1335 Å, and well reproduced in both echelle dispersion modes. In contrast, as in Figure 2, the E140M tracing of α Boo is affected by the pipeline scattered light subtraction at 1206 Å, which has left basically just noise at the location of Si III. Only in the more separated high-dispersion E140H format is the Si III feature recovered. The emission is faint, but still comparable in strength to the C II lines. Note that the Si III 1206 Å profile in β Gem is symmetric, as are the O I 1302 Å, 1304 Å, and 1306 Å triplet components, and C II 1334 Å + 1335 Å; there are slightly redshifted interstellar absorptions in the ground-state transitions, 1302 Å and 1334 Å. In contrast, the Si III, O I, and C II profiles of Arcturus display blueward absorption, symptomatic of the mass outflow. (There also are sharp interstellar medium, ISM, absorptions in the center-left portions of the 1302 Å and 1334 Å ground-state transitions.) The Arcturus spectra also are more affected by fluorescent emissions. Note the stronger S I doublet near 1295 Å, the new pair of lines just shortward of 1334 Å (which are molecular hydrogen emissions pumped by Ly α), and the hump of emission at 1339 Å (which is a conglomeration of carbon monoxide transitions, in the A–X fourth-positive system, fluoresced by the O I triplet).

Table 3
NUV Observations of α Boo

Dataset	UT Start (YYYY- MM-DD)	$T(\text{exp})$ (s)	Aperture ($'' \times ''$)	Grating- CENWAVE (Å)
O4Y701010	1998-08-24	1340	0.1×0.20	E230H-2713
O4Y701020	1998-08-24	2493	0.2×0.06	E230M-2124
O62L02010/20/30	2001-09-03	5715	0.2×0.09	E230H-2762

profiles do not show the same systematic wind asymmetries as α Tau (see Judge & Jordan 1991; Figure 4). This is probably due, in part, to α Boo having lower abundances and a higher wind speed, which places much of the absorption in the far wing of the emission lines. The wavelengths and oscillator strengths are taken from the NIST Atomic Spectra Database (Kramida et al. 2018, and references therein). These lines all have their lower levels in the ground term of each atom or ion, which also dominates the partition functions, so that the population of the lower level tracks the abundance of the species. At the expected densities in the wind, the ground term fine-structure will be populated in a Boltzmann distribution.

The first three terms of Si III are $^1S_{J=0}$, $^3P_{J=0,1,2}$, and $^1P_{J=1}$, and the Si III 1206.5 Å line is the transition from the third to first term, while the semiforbidden 1892 Å transition arises from the second terms. Since there is no radiative cross-talk between the second and third terms (both odd parity), this system can also be accurately treated as a two-level atom.

The first two terms of Mg II are $^2S_{J=1/2}$ and $^2P_{J=1/2,3/2}^o$, and the 2802 Å h line arises from the $^2P_{1/2}^o$ level. The Maxwellian averaged collision strengths, $\bar{\Omega}$ at $T_e = 10,000$ K for electron excitation of the Mg II h 2802 Å line and between the upper levels of the h & k lines have been calculated by Sigut & Pradhan (1995). The h line excitation cross section is in good agreement with the measurements of Smith et al. (1993). Neutral hydrogen collision rates between the upper levels of the h & k lines have been calculated by Monteiro et al. (1988), who found at $T = 5,000$ K $R_{J=1/2 \rightarrow J=3/2} = 3.3 \times 10^{-9} n_{\text{H}} \text{cm}^3 \text{s}^{-1}$. In the low density of the wind, collisional coupling between the upper levels of the Mg II h & k lines is negligible, and the Mg II h 2802 Å scattering can be accurately treated in the framework of a two-level atom. The optical depths in the wind are also too small to thermalize Mg II h 2802 Å by electron collisional de-excitation. Here we consider Mg II h 2802 Å because of its lower optical depth and smaller angular extent on the sky, which makes the STIS aperture

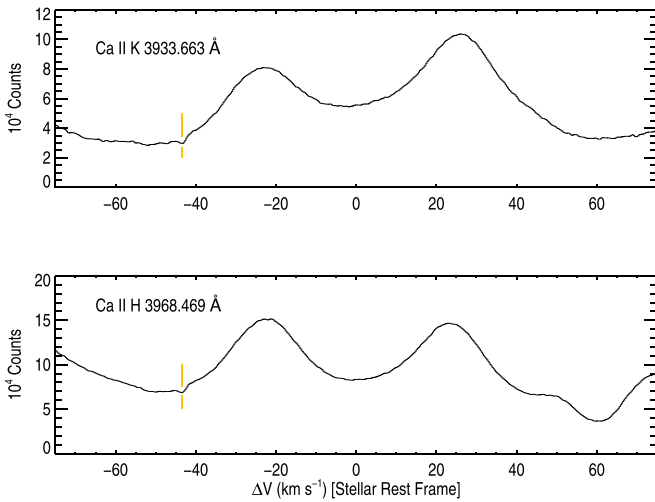


Figure 4. Ca II H & K lines observed with the Harlan J. Smith 107 inch (2.7 m) telescope and cross-dispersed echelle spectrograph (TS21) at McDonald Observatory. The spectra have a resolution of $R \simeq 200,000$ and are the coaddition of spectra obtained on five nights between 2006 January 24–28. There are two velocity bins per resolution element, and the spectra are unsmoothed. The discrete wind absorption feature is seen in both lines near -43 km s^{-1} . Observers: S. Redfield, A. Brown, and G. M. Harper.

correction discussed in Section 3.3.4 smaller, and also reduces the extent of the wind model.

The other lines used in this analysis are slightly more complicated to treat rigorously. The first three terms of C II are ${}^2P_{J=1/2,3/2}^o$, ${}^4P_{J=1/2,3/2,5/2}$, and ${}^2D_{J=5/2,3/2}$. Again, the second and third terms have the same parity, and the upper levels of the semiforbidden (spin-forbidden dipole) C II] 2325 Å Mult. will not have a significant population at wind densities, and can be neglected. However, the 1335 Å triplet lines overlap or share a common upper level. The 1335.708 Å, is blended and shares a common lower level with the weaker 1335.663 Å line (by a factor of nine). We treat this pair as a single transition at 1335.708 Å because the wavelength separation is only 10 km s^{-1} , about half that of the wind turbulence velocity. The 1334.532 Å line is also treated as a single transition, although it shares a common upper level with the weaker 1335.663 Å line. Since the profile modeling is mostly weighted by the shape of the wind scattered absorption, this should not introduce a significant error. A comparison of the two C II lines provides a check on these assumptions (see below in Section 4).

The photons in the lines above are excited by electron collisions, while in cool low-gravity stars like α Boo, the O I 1303 Å triplet is thought to be photoexcited by H Ly β (Haisch et al. 1977; Carlsson & Judge 1993). The O I triplet has a triplet ground state ${}^3P_{J=2,1,0}$ and a single ${}^3S_{J=1}^o$ upper level. The second term, ${}^1D_{J=2}$, may be populated at wind temperatures, and while the triplet emission lines are well separated, there is some overlying emission and opacity from SI UV9 lines. To a much lesser degree, there is also overlying P II opacity. The 1302.168 Å line lacks reflection symmetry in the far emission wings, so we use the 1304.858 Å line to model the wind profile, which is not blended with SI, and we use the 1306.029 Å line as a check. A discussion of emission features in this FUV wavelength region can be found in Carpenter et al. (2018).

3.2. Abundances

Arcturus’ photospheric abundances have been measured by many researchers, and the adopted values for this study are

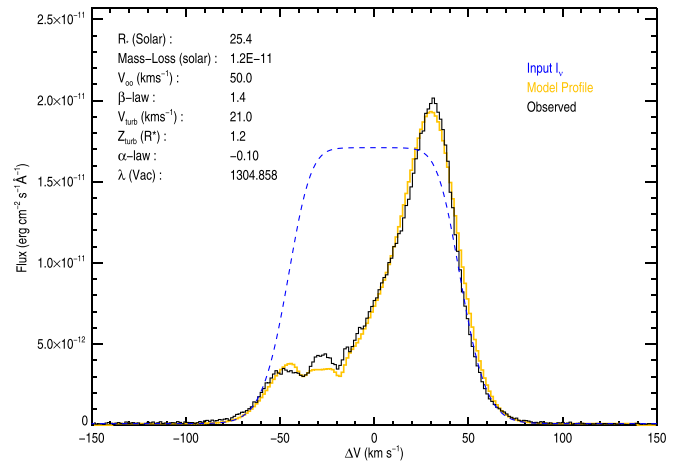


Figure 5. Observed and model line profile for the 2018 O I 1304 Å line in the rest frame of the star.

(The complete figure set (11 images) is available.)

given in Table 1.⁵ For the carbon and oxygen abundances, we adopt those of Ryde et al. (2010), which agree well with those of Abia et al. (2012) and Smith et al. (2013). For silicon and magnesium, we adopt the abundances of Jofré et al. (2015, and references therein).

To obtain a total mass-loss rate from α Boo, the abundance of helium is required, and we adopt the value from Drake (1985).

3.3. Specifying the Wind Properties

The adopted wind velocity properties are described as follows. The functional forms for the outflow speed and turbulence are as complex as can be reasonably justified by the available spectra.

3.3.1. Outflow and Turbulence Velocities

The mean radial flow speed is given by a β -power law

$$V(R) = V_\infty \left[1 - \left(\frac{R_*}{R} \right) \right]^\beta, \quad (2)$$

and the *most probable turbulence velocity* is given by a radial power law

$$V_{\text{turb}}(R) = V_{\text{turb}}(R_{\text{min}}) \left(\frac{R_{\text{min}}}{R} \right)^\alpha. \quad (3)$$

V_{turb} includes the thermal atom and ion motions but is dominated by the nonthermal motions. The modeling parameters are described in Table 4.

The best determined properties are the terminal velocity and the wind turbulence because these shape the blue part of the emission line profile. The photons scattered at these velocities are mostly Doppler redistributed to longer (redward) wavelengths, and the relative opacities are controlled by the four wind and turbulence velocity parameters. Previous attempts by us to model the profiles of strong resonance lines with a constant turbulence gave unrealistic profile shapes, typically

⁵ We use the standard notation of $[A/B] \equiv \log_{10}(A/B)_* - \log_{10}(A/B)_\odot$ to denote the relative abundances of elements A and B as compared to the Sun, and $\log_{10} A(x) \equiv \log_{10}(n_x/n_{\text{H}}) + 12$.

Table 4
Input Parameters for Wind Scattering Models

Parameter	Definition	Comment
R_{\min}	radius at base of wind model	Assumed = $1.2 R_*$
$I_{\Delta\nu}^+(\theta)$	specific intensity at $1.2 R_*$	See Equation (4), shown in plots
\dot{M}	mass-loss rate	Assumed constant and steady
V_∞	terminal wind speed	See Equation (2)
β	power law for wind acceleration	See Equation (2)
$V_{\text{turb}}(R_{\min})$	most probable turbulent velocity	See Equation (3), isotropic
α	power law for turbulence	See Equation (3)

leading to a narrower redward re-emission peak occurring closer to line center. The STIS high spectral resolution reveals the wind sculpting of the absorption profile at small velocity scales that indicate lower turbulence than at the base of the wind, as seen in the lower opacity lines. The inclusion of the α parameter significantly improved the agreement between models and observations.

3.3.2. Radius of the Wind Boundary Condition

The underlying assumption in this analysis is that the wind scattering occurs just above the inhomogeneous chromospheric/transition region photon creation region. However, the spatial extent of cool red giant chromospheres is not well understood (Judge 1986; Section 6.3.4). In a detailed analysis of IUE spectra, Judge (1986) found that including turbulent pressure extension caused by motions indicated by the line widths of the C II] 2325 Å multiplet would lead to an extent of $\Delta H \sim 0.2 R_*$. The unified (chromosphere+wind) model of Drake (1985) also rises to a temperature maximum near $1.2 R_*$. We also note that the α Tau semiempirical chromospheric model by McMurry (1999) has a similar extent. Berio et al. (2011) observed seven K red giants with spectral-types between K0 III and K3 III with CHARA spectro-interferometry. They deduced chromospheric extents from the Ca II IR Triplet lines of between 16% and 47% of the stellar radius. However, as discussed in Harper et al. (2013), it is not clear how robust the uniform disk to limb-corrected radius scaling is, in part, because it is based on a rather compact chromospheric model.

Here we assume that the location of the base of the wind model is $0.2 R_*$ above the photosphere, i.e., at $R_{\min} = 1.2 R_*$, just above the region where atmospheric heating that creates the chromosphere and hotter plasma that is the source of the FUV emission lines. Future high spatial resolution Atacama Large Millimeter/submillimeter Array (ALMA; Carpenter et al. 2020) and next-generation Karl G. Jansky Very Large Array (VLA; Murphy et al. 2018; Petretti et al. 2021) observations will be able to constrain the symmetry and radial extent of the warm partially ionized FUV photon creation region, and significantly improve the constraints on this boundary condition.

3.3.3. Specific Intensity at Boundary Condition

We adopt a schematic form for the specific intensity, $I^+(\Delta\nu)$, at the base of the wind, namely,

$$I^+(\Delta\nu) = S_L [1 - \exp\{-\tau_0 e^{-(\Delta\nu/V_{\text{Dopp}})^2}\}], \quad (4)$$

which represents the intensity from an idealized slab of uniform source function, S_L . Here S_L , τ_0 , and V_{Dopp} are simply treated as parameters to construct a symmetric $I^+(\Delta\nu)$, which matches the observed flux profile in the far red and blue wings. The observed emission lines wings are very nearly symmetric when the observed profile is reflected about the stellar rest velocity. S_L is scaled such that the overall predicted fluxes are close to those observed. In constructing $I^+(\Delta\nu)$, the most important constraint is from the red half of the profile. In the absence of a wind, $I^+(\Delta\nu)$ would become the observed flux profile. Previous wind scattered models have also included a self-reversal in the core lowering the specific intensity there. This has the effect of lowering the wind column density required to match the observed profiles. Our individual line-derived mass-loss rates will be slightly overestimated if such a self-reversal were realistic. Note that the inner boundary has an opaque core of size $R_{\min} > R_*$ so that the most redshifted wind scattered re-emission is blocked by the stellar core and the model line profile in the red-most wing will be slightly underestimated. This does not affect the results of the following modeling.

3.3.4. Note on the Radiative Transfer Solutions

We modeled the wind with 200 shells out to a radius of $100 R_*$ ($2.1''$), with 20 rays intersecting the stellar core of radius R_{\min} , and 25 points interpolated on the rays tangent to the shells in the plane of the sky (see Harper 1994). Two hundred frequency points were used with uniform sampling across the line profile with a resolution of 1.5 km s^{-1} . The formal solution uses the Feautrier scheme, combined with accelerated lambda iteration using a local diagonal operator (Olson et al. 1986). The angular scale of the radiative transfer problem is greater than the angular sizes of the STIS apertures. Therefore, the formal solutions of the radiative transfer equation were mapped onto the sky, and the spectra were extracted for an area corresponding to the angular size of the specific STIS aperture used, centered on the star. We have not attempted to include potential effects such as aperture drift or focus changes that may have occurred during the observations.

Initial spectra were computed for coarse grids of values for the five-fit parameters, and the subsequent grids were refined and re-centered on the previous best-fit values. Integer values for V_∞ and V_{turb} were mostly adopted.

3.3.5. Interstellar Absorption

The observed ground-state resonance line profiles show ISM absorption, which has been accurately measured previously with HST spectra: Mg II and Fe II (Redfield & Linsky 2002), and C II, O I, Al II, and Si II (Redfield & Linsky 2004). These reveal a single ISM component, probably associated with the Gem cloud (Redfield & Linsky 2008), which is characterized by $T_e \simeq 6000 \pm 1100$, and $v_{\text{turb}}^{\text{LISM}} \simeq 1.6 \pm 0.4 \text{ km s}^{-1}$.

Interstellar absorption was included in the synthetic wind scattered profiles, and the spectra were then convolved with the corresponding STIS aperture line spread function (LSF)⁶ before comparing to observations.

⁶ E.g., <https://www.stsci.edu/hst/instrumentation/stis/performance/spectral-resolution>.

Table 5
Ca II and Mg II Discrete Wind Absorption Features

Parameter	Ca II K	Ca II H	Mg II k	Mg II h
	2006 Jan 24–28		2001 Sep 3	
V_{abs} (km s ⁻¹)	-43.3 ± 0.1	-43.4 ± 0.1	-48.2 ± 0.1	-48.0 ± 0.1
V_{mpv} (km s ⁻¹)	~0.5	~0.4	2.6 ± 0.1	2.3 ± 0.1
N_{ion} (cm ⁻²)	3.1 × 10 ¹⁰	3.7 × 10 ¹⁰	1.7 × 10 ¹²	1.5 × 10 ¹²

3.4. Discrete Wind Absorption Features

The 2001 Mg II h & k profiles reveal a narrow discrete absorption feature at -48 km s⁻¹ (O’Gorman & Harper 2011). To estimate the feature properties, we modeled a single Gaussian absorption feature against a somewhat uncertain background flux profile. We then deconvolved the implied *most probable velocity*, V_{mpv} , with the E230H 0.2 × 0.09 aperture ($R \sim 114,000$) LSF assuming both are Gaussian. The feature minimum velocity, V_{abs} , the deconvolved V_{mpv} , and the ion column density are given in Table 5. A comparison of the results for the two lines gives a better estimate of the uncertainty than the formal fitting uncertainties. The 1998 profiles do not show clear absorption, but the flux profile shows structure near this velocity.

Observations of the Ca II H & K lines obtained at McDonald Observatory between 2006 January 24–28 at higher spectral resolution ($R \simeq 200,000$) are shown in Figure 4. The properties for these lines are also given in Table 5. These discrete wind lines have very small measured widths that are close to the instrumental resolution and the deconvolution, which assumes a Gaussian LSF, is uncertain. We cannot put spatial constraints on the absorbing ions, i.e., they could be close to, or far from the star. Calcium can be photoionized by the strong hydrogen Lyman lines (Athay & Zirker 1962) and is expected to be in Ca III in the base of the wind (Harper et al. 2004). The recombination to Ca II is expected to occur far from the star when adiabatic cooling becomes important, and the very low turbulence probably reflects conditions in the far wind.

We also included some narrow discrete absorption features, where possible, in the Mg II h 2802 Å and O I model profile fits.

4. Results

The results of the wind scattering computations are given in Table 6, and the line profiles are shown in Figure 5 (panels 5.1 through 5.11). The mass-loss rate given for each line assumes that all of the element is in the given ionization state, with the abundances in Table 1. For each line, the wind fit parameters were unconstrained from each other to provide an indication of the systematic uncertainties. Most fit parameters are correlated, and experimentation reveals that simultaneous changes of 10% in the fits parameter, and 0.2 in α , and 0.2 in β can lead to profiles that appear very similar. We therefore adopt these as typical “fit” uncertainties for each line. Changes of ±2 km s⁻¹ in $V_{\infty} + V_{\text{turb}}$ can easily be accommodated by changes in β and α , or the assumed input profile. Such changes can also lead to 10% changes in the mass-loss rate. These values are intended to guide the reader, and are not a rigorous analysis of the interplay of input profiles and fit parameters.

Figure 5 (panels 5.1 through 5.6) shows the observed and modeled O I 1304 Å and O I 1306 Å profiles for the 2018, 2019, and 1998 epochs. The appearance of narrow additional absorption on top of the broad wind-induced asymmetry is apparent, and it changes between the 2018 and 2019 epochs.

Table 6
 α Boo: Results of Wind Scattering Models

Transition (Å)	\dot{M} ($M_{\odot} \text{ yr}^{-1}$)	V_{∞} (km s ⁻¹)	β	$V_{\text{turb}}(R_{\text{min}})$ (km s ⁻¹)	α
Si III 1206.5 (2018/2019)	1.0 × 10 ⁻¹²	48	Unc.	Unc.	-0.10
O I 1304.8 (1998)	1.0 × 10 ⁻¹¹	52	1.5	22	-0.20
O I 1304.8 (2018)	1.2 × 10 ⁻¹¹	50	1.4	21	-0.10
O I 1304.8 (2019)	1.2 × 10 ⁻¹¹	49	1.5	22	+0.00
O I 1306.0 (1998)	0.7 × 10 ⁻¹¹	48	2.0	18	-0.20
O I 1306.0 (2018)	1.4 × 10 ⁻¹¹	53	1.7	24	-0.15
O I 1306.0 (2019)	1.4 × 10 ⁻¹¹	50	1.9	21	+0.20
C II 1334.5 (2018/19)	2.6 × 10 ⁻¹¹	51	1.4	23	+0.38
C II 1335.7 (2018/19)	2.6 × 10 ⁻¹¹	51	1.3	22	+0.40
Mg II 2802.7 (1998)	1.1 × 10 ⁻¹¹	44	1.7	24.5	+0.35
Mg II 2802.7 (2001)	9.5 × 10 ⁻¹²	41	1.6	25.5	+0.37

Note. The mass-loss rates shown here assume that all of the element is in the given ionization state with the abundances given in Table 1.

Consideration of the overall profiles of the three epochs of the high S/N O I diagnostic reveals consistent wind behavior between the two lines and between the different epochs. Since the wind sampled by each line for a given epoch will be the same, differences in the fit parameters give an indication of the systematic errors. The O I 1306 Å line has a Si I blend at 1305.88 Å, and is narrower with the wind absorption lying on the edge of the emission core, making it potentially less reliable than the properties derived from the O I 1304 Å line.

The O I mass-loss rates from the 2018 and 2019 epochs are very similar, and we adopt an average $\dot{M} = 1.3 \pm 0.1 \times 10^{-11} M_{\odot} \text{ yr}^{-1}$. Here (\pm) indicates the average range, about the mean value, and is not a statistical 1σ . The mean terminal velocity is $\overline{V_{\infty}} = 50.5 (\pm 2.0)$ km s⁻¹, with $\overline{\beta} = 1.63 (\pm 0.25)$. The fit parameters that describe the line width at a particular radius give $\overline{V_{\text{turb}}} = 22.0 (\pm 1.5)$ km s⁻¹ and $\overline{\alpha} = 0.0 (\pm 0.2)$. These ranges are consistent with fit uncertainties suggesting that the large-scale flow did not change significantly between the 2018 and 2019 epochs, while the underlying emission strength changed slightly and the discrete narrow wind absorption also changed. The 1998 epoch has a slightly smaller O I mass-loss rate but the properties are otherwise similar. Because the individual wind fit properties of each O I line for the 2018 and 2019 epochs are very similar, except perhaps for the O I 1306 Å α s, the mean O I 1304 Å and O I 1306 Å α s differ by only 0.05. In the following, we combine the 2018 and 2019 epoch spectra for the lower S/N Si III and C II lines.

Figure 5 (panel 5.7) shows the observed and modeled Si III 1206.5 Å line profile. The shallower asymmetry and lower S/N of the Si III 1206.5 Å line means that some wind properties are

not as tightly constrained (marked as Unc. in Table 6), but the terminal velocity is similar to O I. The noticeable difference is the lower mass-loss rate. An ISM feature is tentatively detected near -6 km s^{-1} , similar to the ISM absorption observed in other singly ionized species.

Figure 5 (panels 5.8 and 5.9) show the observed and model C II 1334 Å and C II 1335 Å line profiles. The two C II lines present almost identical wind parameters, which indicates that the ETLA approximation for these lines is reasonable. The value of V_{turb} is the same as the mean value for the O I lines, while the turbulence declines significantly more rapidly with radius, i.e., $\bar{\alpha} \simeq 0.39$.

Figure 5 (panels 5.10 and 5.11) shows the two Mg II h 2802 Å lines from 1998 and 2001. These also have very similar wind properties to each other. These are the most opaque transitions and sample the outermost wind. The terminal velocity $\bar{V}_{\infty} = 42.5 (\pm 1.5) \text{ km s}^{-1}$ and $\bar{\beta} = 1.65$. For both profiles, there is a small profile mismatch near -36 km s^{-1} , and also where extra narrow absorption is present near -48 km s^{-1} in 1998. The optical depth in the Mg II h line is sufficiently large that some of the wind scattered emission is not collected in the STIS apertures. Neglect of this correction leads to noticeable changes in the derived mass-loss rate, because the emission excluded by the aperture occurs near zero velocity.

To within the modeling uncertainties, the two most opaque diagnostics, C II and Mg II, both share the same radial turbulent velocity decline, which is quite different to O I, which presents an almost constant value at 22 km s^{-1} . The HST observation of the chromospheric C II] 2325 Å electron-density sensitive multiplet shows a smaller turbulence where $V_{\text{turb}}(\text{Chrom}) \simeq 14 \text{ km s}^{-1}$.

The approximate radii (depending on model) where the maximum optical depth, as a function of velocity, $\tau_{\Delta V} = 0.5$ for Si III 1206.5 Å, O I 1304 Å, C II 1334 Å, and Mg II h 2802 Å are $\sim 3, 15, 30,$ and $50 R_{*}$, respectively. These values give a rough indication of the maximum radii where the wind models have sensitivity to those individual diagnostics. The trend of α is such that the lines sampling the wind closest to the star indicate a near constant value, of $\alpha \simeq 0$, which then increases to $\alpha \simeq 0.4$ at large distances. This might indicate that the adopted form for the turbulence given in Equation (3) is oversimplified, or that the physical meaning and interpretation of line-of-sight microturbulence change as the densities and spatial scales change, and the spatial correlations cannot be ignored (Böger et al. 2003).

5. Interpretation of the Wind Properties

The mass-loss rate for each line presented in Table 6 assumes that all of the element is in the given ionization state, with the abundances given in Table 1, and that the populations of the lower levels have a Boltzmann distribution. The immediate result from this modeling is that there is significantly less Si III present than the other species, indicating that it is a minority species.

A comparison of the mass-loss rates derived from different species gives an estimate of the ionization fraction for each element, which in turn provides a characteristic wind temperature and thus a total mass-loss rate from α Boo. Using the abundances in Table 1, the wind properties presented in Table 6, and approximate static ionization balances points to a wind temperature of $T_{\text{wind}} \sim 10,000\text{--}20,000 \text{ K}$. Under these conditions, the Boltzmann assumption is reliable, and at $1.2 R_{*}$ the dynamical timescale, r/v , is not negligible compared to

characteristic radiative recombination timescales. Flow advection of the ionization must be considered. Judge (1986, Section 5.4.X) examined the ionization balance in the chromosphere of α Boo and found that the ionization balance of O I and O II is controlled by charge-exchange reactions with hydrogen. The charge-exchange recombination and ionization with neutral hydrogen and protons, respectively (Field & Steigman 1971; Stancil et al. 1999), dominate other ionization and recombination processes. The balance is approximately given by

$$\frac{n(\text{O II})}{n(\text{O I})} \simeq \frac{8}{9} \frac{n(\text{H II})}{n(\text{H I})} \exp^{-227/T}$$

where, for typical wind temperatures, the ratio is close to the statistical weights of the output channels. Baliunas & Butler (1980) pointed out the importance of charge-exchange for Si III ionization in the temperature range $T = 15,000\text{--}60,000 \text{ K}$ in the atmospheres of cool stars. At the expected wind temperatures, helium is predominately neutral, and if the ionization balance is dominated by hydrogen charge-exchange (Clarke et al. 1998), the ionization balance is given by

$$\frac{n(\text{Si III})}{n(\text{Si II})} \simeq \frac{1}{3} \frac{n(\text{H II})}{n(\text{H I})} \exp^{-31,796/T}.$$

The ionization balances of Mg II and Mg III, and C II and C III are closer to the *coronal approximation*, the low-density limit balance of electron collisional ionization and radiative and dielectronic recombination (Arnaud & Rothenflug 1985, and references therein). The different temperature dependence of the O I and Si III populations provides the sensitivity to constrain the wind temperature in the Si III wind scattering region, close to the star.

To find the ionization balance for the wind diagnostics, we first solve the wind advection statistical equilibrium equations for hydrogen (Weymann 1962; Glassgold & Huggins 1986) using the two-stage ionization process described by Hartmann & Avrett (1984). At chromospheric temperatures, the $n = 2$ level is populated by electron collisions and scattered H I Ly α , followed by photoionization by the optically-thin Balmer continuum. We approximate the radial mean intensity

$$J_{\nu}(z) = W_{\text{LD}}(z) B_{\nu}(T_{\text{Balmer}}), \quad (5)$$

where T_{Balmer} is the mean Balmer continuum radiation temperature, and the geometric term $W_{\text{LD}}(z)$, where $z = R/R_{*}$, is analogous to the standard radiation dilution factor but explicitly includes the linear limb-darkening model of $I(\mu) = I(\mu = 1) [1 - c(1 - \mu)]$. The u and U photometric band coefficients of Claret & Bloemen (2011) have $c \simeq 1$, giving $I(\mu) \simeq I(1)\mu$. The functional form for W_{LD} for this limb-darkening law is given in the Appendix. T_{Balmer} is found by combining the spectrophotometry of Burnashev (1985) and the ASTRAL HST NUV and FUV fluxes, and for this limb-darkened model we obtain $T_{\text{Balmer}} = 3890 \text{ K}$. For the hydrogen electron collisional excitation and ionization rates, we adopt those of Scholz & Walters (1991), and assume a fixed additional electron contribution from metals of $x_{\text{met}} = n_e/n_{\text{H}} = 5 \times 10^{-4}$. We treat the radiative recombination to the $n = 1$ ground state with escape probabilities (see Canfield & Ricchiazzi 1980), and the recombination to higher levels is assumed to be optically thin, i.e., intermediate between the classical Case A and B recombination

rates. We also treat Ly α with escape probabilities. For the lower boundary, we initialize the ionization balance with the static values. The hydrogen solution provides the required neutral hydrogen, proton, and electron densities to solve for the ionization balance for the UV diagnostics.

At the base of the wind, the oxygen and silicon ionization balance is intimately coupled through the charge exchange with neutral hydrogen and protons. If the total oxygen abundance can accurately be given by O I and O II, and that of silicon by Si II and Si III, then the ratio of fractional number densities is

$$\frac{n_{\text{OI}}/A_{\text{O}}}{n_{\text{Si III}}/A_{\text{Si}}} \simeq \frac{1 + (n(\text{H II})/n(\text{H I}))3 \exp\{+31,769/T_{\text{wind}}\}}{1 + (n(\text{H II})/n(\text{H I}))(8/9) \exp\{-227/T_{\text{wind}}\}}. \quad (6)$$

When $n(\text{H II})/n(\text{H I}) \gg 1$, i.e., when the hydrogen in the wind is dominantly ionized, this expression reduces to

$$\frac{n_{\text{OI}}/A_{\text{O}}}{n_{\text{Si III}}/A_{\text{Si}}} \simeq \frac{27}{8} \exp\{+32023/T_{\text{wind}}\}, \quad (7)$$

and the variations of the wind temperature can, in principle, be estimated as a function of radius by comparing the individual ion densities derived from the line modeling.

To evaluate the wind temperature in the Si III 1206.5 Å scattering region, the hydrogen advection ionization balance was solved for a grid of mass-loss rates and constant temperatures. The hydrogen solutions were then used to evaluate the ionization balances for all of the diagnostics near $2R_*$. The ionization balance as a function of radius can be deduced from Equations (6) and (7), which, when $n(\text{H II})/n(\text{H I}) > 1$, show that it is approximately constant for the isothermal cases considered here. The ionization balance for Mg III/Mg II and C III/C II are close to the *coronal approximation*, which is independent of the electron density, and again constant in radius for the isothermal case. The ionization balances were then used to convert the diagnostic-specific mass-loss rates in Table 6 to ionization-corrected mass-loss rates. These are shown in Figure 6. From this, we derive a weighted base wind temperature of $\sim 15,400$ K, where hydrogen is significantly ionized, i.e., $n(\text{H II})/n(\text{H I}) > 1$, and a mass-loss rate of $2.5 \times 10^{-11} M_{\odot} \text{ yr}^{-1}$. Ignoring the noncontemporaneous Mg II results would give $T_{\text{wind}} \sim 14,500$ K. The indicated (shaded) uncertainties are from the adopted abundances and do not include fit the uncertainties described previously. The adoption of a mean base wind temperature introduced an additional uncertainty.

With this mass-loss rate, wind temperature, and hydrogen ionization balance, the radio free-free continuum spectrum can be computed and compared to the high-quality multiwavelength VLA continuum observations of α Boo (O’Gorman et al. 2013). The significant increase in bandwidth of the upgraded VLA means that these observations provided, for the first time, high S/N fluxes for a sweep of wavelengths (0.7 \rightarrow 20 cm) obtained at similar epochs for the single K red giants Arcturus (alpha Boo) and Aldebaran (alpha Tau). Previously only a handful of low S/N fluxes at a few wavelengths were available (Drake & Linsky 1986a, and references therein). The radio opacity is proportional to the electron density squared, i.e., $\kappa_{\nu} \propto n_e^2$, so these data provide a robust check on the present HST-STIS wind scattering analysis. To compute the full radio spectrum, we also require a description of the chromospheric material beneath $1.2R_*$. We

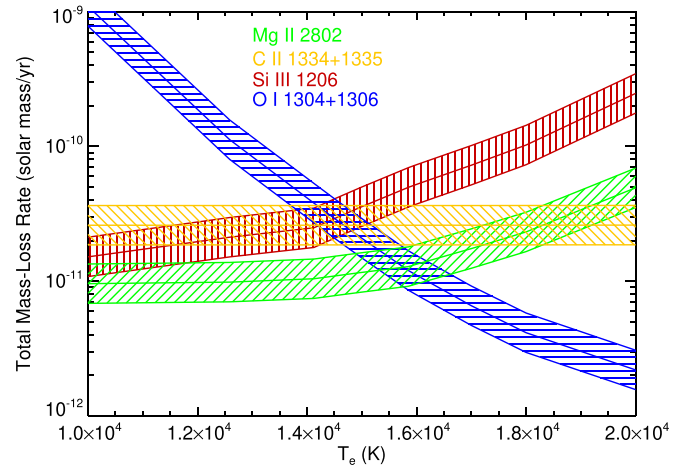


Figure 6. Inferred mass-loss rates from models of different ions as a function of wind temperature near $2R_*$. The hatched region indicates the typical 1σ abundance uncertainty. The optimum solution is $T_{\text{wind}} \simeq 15,400$ K, and $\dot{M} \simeq 2.5 \times 10^{-11} M_{\odot} \text{ yr}^{-1}$. The C II is assumed to be the dominant ionization state at 10^4 K and is insensitive to the mass-loss rate in this limited temperature range. The Mg II curve lies below the data collected for this project and is from 1998 and 2001. The opposing trends of Si III and O I provide a tight temperature constraint, while the mass-loss rate is more uncertain.

adopt the chromospheric model of Ayres & Linsky (1975). This chromospheric model is rather compact and does not include a turbulent pressure extension term, so we increase the local density scale height to extend the model to $1.2R_*$, while conserving the volume emission measures. We solve the spherical radio free-free radiative transfer problem using the *gaunt factors* from Hummer (1988). The results are shown in Figure 7. The HST model for 2018 + 2019 slightly underpredicts the fluxes obtained in 2011 + 2012 for the L and S bands, the ones most sensitive to the conditions within the wind. Increasing the wind temperature to 18,000 K, or increasing the mass-loss rate to $4 \times 10^{-11} M_{\odot} \text{ yr}^{-1}$, brings the 2018 + 2019 epoch results into agreement with the 2011 + 2012 epoch radio observations. A combination of changes in T_{wind} and \dot{M} would also work. Because of the lower S/N of the older VLA C-band radio measurements, it is difficult to establish the degree of radio variability and its implications for wind variability.

6. Wind Acceleration, Turbulence, and Alfvén Wave Amplitudes

The line profile analysis provides new quantitative evidence for the radial distribution of wind turbulence in a single red giant throughout the wind acceleration region. In this section we explore how these data can constrain the properties of Alfvén wave-driven winds, a leading candidate for driving the stellar outflow. This section is structured as follows: First, the radial distribution of turbulence predicted by WKB Alfvén wave-driven wind theory is compared to the empirical HST-STIS constraints on V_{∞} and β , and then independently V_{turb} and α . Second, the rate of implied wave damping is derived, and third, the thermal consequences of this wave heating in the wind are examined.

In particular, we examine if the derived wind acceleration and turbulence are compatible with Alfvén wave-driven winds in the framework of a steady (stationary) flow, in which case the use of a time-averaged wave force requires the wave periods, P_w , to be small compared to the dynamical flow timescale, τ , for the wind to cover a density scale height,

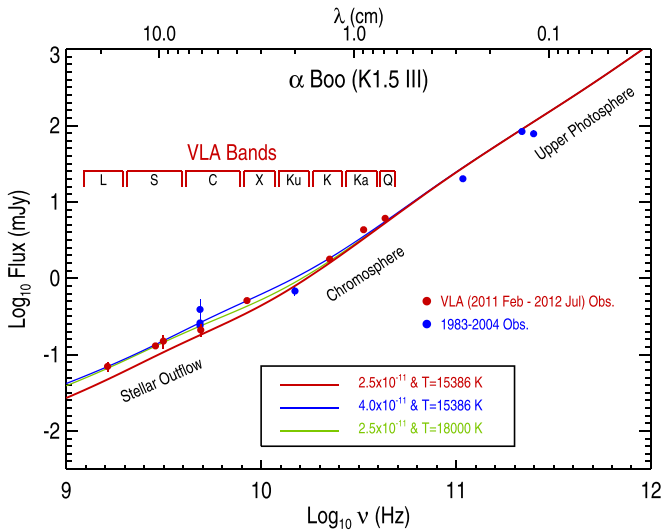


Figure 7. The radio spectrum computed from the wind model derived from the HST-STIS UV wind scattering line analysis. The red curve is the new model prediction, and the circles and error bars are the recent VLA observations (O’Gorman et al. 2013). The blue circles are older VLA and other measurements, and the regions probed by the different VLA bands are annotated. The nominal model underestimates the epoch 2011–2012 VLA fluxes, but by either increasing the temperature to 18,000 K (green), or the mass-loss rate to $\dot{M} = 4.0 \times 10^{-11} M_{\odot} \text{ yr}^{-1}$ (blue) brings the models and observations into agreement.

namely

$$\tau = \frac{r}{V} \left(2 + \frac{d \ln V}{d \ln r} \right)^{-1}.$$

For the wind flow derived above, $\tau > 6$ days for $R < 25 R_{*}$, so the wave periods should satisfy $P_w \leq 6$ days.

6.1. Wave Amplitudes

The semiempirical approach adopted here was first applied to IUE spectra of lower-gravity ζ Aur eclipsing binary systems by Kuin & Ahmad (1989): 32 Cyg (K4 Ib + B7 V), ζ Aur (K4 Ib + B5 V), 22 Vul (G3 Ib-II + B9), and 31 Cyg (K4 Ib + B4). In these systems, the turbulent velocities have been derived from curve-of-growth analyses at different projected heights during atmospheric eclipses. Typical IUE most probable velocities along the direction perpendicular to the radial direction show an increase in the wind acceleration region reaching $\sim 20\text{--}30 \text{ km s}^{-1}$ at $2.5 R_{*}$, and continuing to increase outwards (Kuin & Ahmad 1989, and references therein). Subsequent detailed 2D radiative transfer line profile modeling of high S/N and high spectral resolution HST-GHRS spectra revealed lower values with an assumed isotropic most probable velocity of 20 km s^{-1} at $1.2 R_{*}$, declining to 15 km s^{-1} at $2.5 R_{*}$ for ζ Aurigae (Baade et al. 1996).

Our power-law parameterization given in Equation (3) cannot capture an initial increase and subsequent decline, and the HST-STIS spectra do not fully justify two additional fitting parameters in the line fits. However, by comparing the results from different lines, some additional clues present themselves. The O I lines show a flat turbulence with $V_{\text{turb}} \sim 22 \text{ km s}^{-1}$, while the C II and Mg II lines, which sample the far reaches of the stellar wind, suggest similar turbulence at the base of the wind but then decline with $\alpha \simeq 0.4$. Combined, these data suggest that the turbulence near the star is supersonic and

initially constant, but then decreases outward beyond some radius.

The turbulence fit for Si III 1206.5 Å is not strongly constrained because of the lower S/N and only a single line fit. Unfortunately, other lower opacity lines such as the numerous UV Fe II emission lines and Si II 1808 + 1816 Å triplet are not suitable for wind profile modeling and do not provide additional constraints.

Damped WKB Alfvén wave-driven models using the theory developed from earlier solar work by Hartmann & MacGregor (1980) show that the rms Alfvén wave amplitude tangential to the radial field direction, i.e., $\sqrt{\langle \delta v_{\perp}^2 \rangle}$, initially increases with radius as the density decreases. Then exterior to the Alfvén wave critical point near $1.75 R_{*}$ (i.e., the small Alfvén Mach number limit cold undamped wave-driven wind solution of Holzer et al. 1983), the wave amplitude declines as the waves are damped by ion-neutral collisions (Hartmann et al. 1982; Hartmann & Avrett 1984). Hartmann et al. (1982) pointed out that the wave amplitude at the critical point

$$\sqrt{\langle \delta v_{\perp}^2 \rangle} \sim v_{\text{esc}}(z_{\text{crit}}) / (1 + z_{\text{crit}} / \lambda),$$

where λ is an assumed constant Alfvén wave-damping length in units of stellar radius in this formalism. If we take $z_{\text{crit}} \simeq 1.75$ and $\lambda = 1$, then we find for α Boo $\sqrt{\langle \delta v_{\perp}^2 \rangle} (1.75 R_{*}) \sim 34 \text{ km s}^{-1}$.

Relating these theoretical rms wave amplitudes to observable parameters such as the isotropic most probable velocity that defines the V_{turb} in this work is nontrivial and approximate, representing temporal averages of wave shape and projection, combined with thermal motions (see, for example, Worrall & Wilson 1973; Oster & Ulmschneider 1973; Beckers 1976). Hartmann et al. (1982) adopted correspondences between $\sqrt{\langle \delta v_{\perp}^2 \rangle}$ and V_{turb} in the range

$$\sqrt{3} V_{\text{turb}} < \sqrt{\langle \delta v_{\perp}^2 \rangle} < 2\sqrt{2} V_{\text{turb}}. \quad (8)$$

Jordan et al. (1984, as cited in Jordan 1986) suggested $\sqrt{\langle \delta v_{\perp}^2 \rangle} \simeq \sqrt{3/2} V_{\text{turb}}$.⁷ These correspondences are consistent with the values of V_{turb} found here, namely $V_{\text{turb}} = (0.35 \rightarrow 0.82) \sqrt{\langle \delta v_{\perp}^2 \rangle}$ or $V_{\text{turb}} \simeq 0.6 \sqrt{\langle \delta v_{\perp}^2 \rangle}$, which would give $V_{\text{turb}}(1.75 R_{*}) \sim 20 \text{ km s}^{-1}$.

The wave energy density, ϵ , for WKB Alfvén waves is given by

$$\epsilon(r) = \rho(r) \langle \delta v_{\perp}^2(r) \rangle, \quad (9)$$

and the time-average force per unit volume, f_w , is given by $f_w = -(1/2) d\epsilon/dr$. In the following, we consider a radial outflow in a geometry where flux tubes may be diverging in the thin-flux-tube approximation. The radial momentum equation is given by

$$V \frac{dV}{dr} = -\frac{1}{\rho} \frac{d}{dr} \left(P_{\text{gas}} + \frac{\epsilon}{2} \right) - \frac{GM_{*}}{r^2} \quad (10)$$

(Hartmann & MacGregor 1982), so with our semiempirical estimates for the wind acceleration, dV/dr , and gas pressure, P_{gas} , from the HST-STIS analysis, and the relatively well-

⁷ In their study of ζ Aur systems, Kuin & Ahmad (1989) simply adopted $\sqrt{\langle \delta v_{\perp}^2 \rangle} \simeq V_{\text{turb}}$

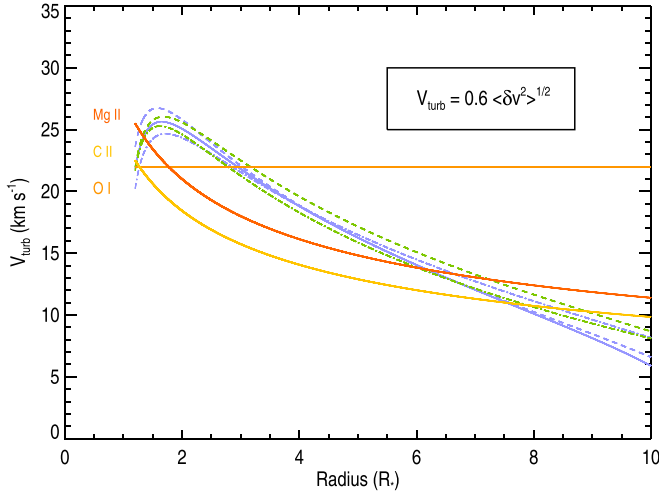


Figure 8. The turbulent velocities (most probable) inferred from the HST line profile analysis (solid gold, orange, red), and that required to drive the inferred wind acceleration (green and blue curves) for $V_{\infty} = [44, 49, 55]$ and $\beta = [1.3, 1.5, 1.7]$ derived from Equations (10) and (9). The blue curves are for $V_{\infty} = 49 \text{ km s}^{-1}$ and $\beta = [1.3, 1.5, 1.7]$, and the green curves are for $\beta = 1.5$ and $V_{\infty} = [44, 49, 55] \text{ km s}^{-1}$. The dashed curve is for the smaller value of the variable, while the dotted–dashed curve is for the higher value. The two sets of curves are independent, one (solid: gold, orange, and red) being semiempirical, and the other (blue and green) being theoretical. To compare the two, we have assumed $V_{\text{turb}} = 0.6\sqrt{\langle \delta v_{\perp}^2 \rangle}$.

determined stellar parameters, R_* and M_* , we can solve Equation (10) for $\epsilon(r)$. From this, we can then derive the run of $\sqrt{\langle \delta v_{\perp}^2 \rangle}$ (from Equation (9)) required to accelerate the wind according to a nominal value of β -power law of $\beta \simeq 1.5$.

For each value of derived V_{∞} and β , there is a very small range of boundary condition values for $\sqrt{\langle \delta v_{\perp}^2 \rangle}$ at $1.2 R_*$ that lead to sensible values over the first $10 R_*$, i.e., within the range $1 < \sqrt{\langle \delta v_{\perp}^2 \rangle} < 50 \text{ km s}^{-1}$. Note that beyond $10 R_*$, these solutions do not have much meaning because the wind is unlikely to be closely represented by a β -power law. Assuming an isothermal wind of $15,400 \text{ K}$ and stellar parameters in Table 1, we find $\sqrt{\langle \delta v_{\perp}^2(1.2 R_*) \rangle} = 38 \text{ km s}^{-1}$. With the nominal conversion factor: $V_{\text{turb}}^{\text{WKB}} = 23 \text{ km s}^{-1}$, consistent with the observed values. In Figure 8 we also show the run of wave amplitudes (converted to V_{turb} by multiplying by 0.6) for models with $V_{\infty} = [44, 49, 55]$ and $\beta = [1.3, 1.5, 1.7]$. These all show an initial increase as the wind accelerates, followed by a decrease required to match observed terminal velocities, recalling that undamped wave models lead to excessive terminal flow speeds. Figure 8 shows that the theoretical turbulence is not incompatible with constraints from the line profile models. This behavior might explain the difference between the inner constant turbulence from O I and subsequent decline deduced from C II and Mg II. An initial rise in turbulence and then decline might result in an apparent inner constant value. Given that one set of curves is derived from the 1D momentum equation with the derived wind acceleration and the other curves are derived from line profile fits, the agreement between the two is surprisingly good.

Note that these constraints on $\sqrt{\langle \delta v_{\perp}^2 \rangle}$ assume WKB wave properties, through Equations (9) and (10), but not a specific value of the radial magnetic field; however, they do implicitly assume that $\sqrt{\langle \delta B_{\perp}^2 \rangle} < B/2$ to avoid strong nonlinear damping (Hollweg 1971; Belcher & Davis 1971; Andreev et al. 1997).

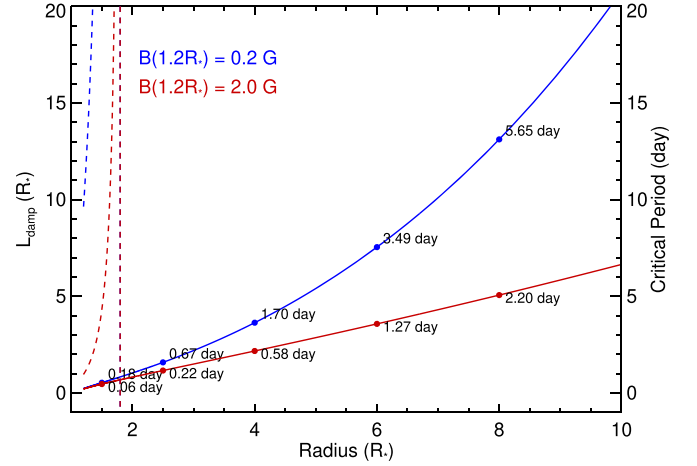


Figure 9. The semiempirically derived damping lengths in the frame of the star (solid lines) for assumed magnetic field strengths at $1.2 R_*$ of 0.2 G (blue) and 2.0 G (red). The increase in damping length with radius is opposite to that expected from ion-neutral damping of monochromatic Alfvén waves. The corresponding wave periods under the assumption of weak ion-neutral damping in a locally homogeneous atmosphere are also given at selected radii. The dashed lines show the critical wave periods (shown on the right y-axis) for wave reflection for the wind model, as discussed in Section 7.1. Periods longer than these critical periods will undergo partial wave reflection, but some energy can still propagate into the outer regions.

6.2. Wave Damping

The gradient of the wave energy density also places constraints on the damping of the waves that drive the wind. Assuming a radial magnetic field, $B(r)$, the wave damping length in the inertial frame of the star, $L(r)$, can be derived from the Conservation of Wave Action Density generalization to include dissipation (Jacques 1977; Bretherton & Garrett 1968) giving

$$\frac{1}{L(r)} = -\frac{d}{dr} \ln\{\epsilon(r)M_A(1 + M_A^2)\} \quad (11)$$

(Hartmann & MacGregor 1980), where the Alfvén wave Mach number, M_A , is the ratio of the wind velocity, $V(r)$, to the Alfvén wave velocity, $V_A = B/\sqrt{4\pi\rho_{\text{eff}}}$, i.e., $M_A = V/V_A$. ρ_{eff} is the effective gas density sensed by the waves (see Holzer et al. 1983, Appendix A10), and because of the rapid hydrogen-proton momentum exchange, $\rho_{\text{eff}} \simeq \rho_{\text{gas}}$ at the base of the wind for ionization conditions of interest.

Since the wind velocity, turbulent velocity, and gas density have been derived as a function of radius from the UV line profile analysis, $L(r)$ can be semiempirically constrained if we assume a spatially independent constant (correspondence) relating $\sqrt{\langle \delta v_{\perp}^2 \rangle}$ to V_{turb} . The results are shown in Figure 9 for two values of the magnetic field at the base of the wind: $B(1.2 R_*) = 0.2$ and 2.0 Gauss. The damping lengths increase with increasing radius and are of the order of the stellar radius within a few stellar radii above the photosphere.⁸ Previous Alfvén wave–driven wind models for stellar parameters similar to red giants have adopted surface magnetic fields of $B(R_*) = 10 \text{ G}$ (Models 16–18: Hartmann & MacGregor 1980) and $B(R_*) = 2\text{--}10 \text{ G}$ (Krogulec 1988), and in these circumstances, the wind flow near the star is sub-Alfvénic, $M_A \ll 1$.

⁸ The damping lengths shown in Kuin & Ahmad (1989) appear to have a sign error in their numerical evaluation of the damping lengths, and are thus shown too small. However, they do show the same trend with radial increase.

Once the wind speed approaches V_∞ , Equations (11) and (3) give

$$L \sim \frac{z}{2\alpha + 1}, \quad (12)$$

where α is the radial turbulence power law. This explains the damping length linear trend in Figure 9 for $B(1.2R_*) = 2$ G, but for a smaller magnetic field, $B(1.2R_*) = 0.2$ G M_A is no longer $\ll 1$, and the trend is no longer as linear.

For the case where the wave energy is strongly peaked at a single frequency, one would expect the ion-neutral damping length to decrease, i.e., the damping rate increases, as the wind density decreases, and the mean collision time between ion and neutral collisions increases (Hartmann & MacGregor 1980; Piddington 1956). This is opposite to the trends shown in Figure 9. At 15,400 K, the major constituents of α Boo’s wind are protons, electrons, neutral hydrogen, and helium atoms. Collisions between the neutral species and the protons, which are tied to the magnetic wave fluctuations, damp the Alfvén waves. In Figure 9 the period of monochromatic waves that would produce the semiempirical determined values of $L(r)$ is annotated, following the generalized damping-rate prescription of Holzer et al. (1983, Appendix A) with the $H^+ + H$ momentum transfer rate coefficient from Glassgold et al. (2005). The assumption of locally weak damping in a homogeneous medium may not be fully satisfied in this wind, and these values should be regarded as indicative.

6.3. Energy Balance

Next, we turn our attention to the implied heating in the stellar wind and compare the expected temperatures to our semiempirical temperature for the base of the wind. With the derived damping lengths, L , the wave dissipation heating rate, Q , can be found from

$$Q(r) = \frac{\epsilon(v + V_A)}{L}, \quad (13)$$

e.g., Falceta-Goncalves et al. (2006), where we have dropped the radial dependence of each term on the right-hand side for clarity. In the following, we use the density structure for $\dot{M} = 2.5 \times 10^{-11} M_\odot \text{ yr}^{-1}$. In Figure 10 the quantity Q/n_H^2 is shown for $B(1.2R_*) = 2$ G for $V_\infty = [44, 49, 55]$ and $\beta = [1.3, 1.5, 1.7]$ (green and blue lines), and also for the run of $\epsilon(r)$ derived for $\beta = 1.5$ and $\alpha = 0.35$ for 0.3 G (gold) and 2 G (red). The different results for 2 G cases result mainly from the differences in the runs of microturbulence: the solid gold and red curves are from the assumed α -power-law form, while the blue and green curves are derived from Equation (10).

For the estimated wind temperature, hydrogen is at least 50% ionized, so $n_e \simeq 0.5 n_H$, so that the quantity Q/n_H^2 can be compared to the radiative power loss curve, $P_{\text{rad}}(\text{erg cm}^{-3} \text{ s}^{-1})$, where the total power loss per unit volume is $n_e n_H P_{\text{rad}}$. The solar P_{rad} computed with the coronal approximation has two peaks corresponding to H Ly α near 16,000 K, with $P_{\text{rad}} \simeq 3 \times 10^{-22} (\text{erg cm}^{-3} \text{ s}^{-1})$, and to C III near 10^5 K with $P_{\text{rad}} \simeq 6 \times 10^{-22} (\text{erg cm}^{-3} \text{ s}^{-1})$; Landi & Landini (1999). For cool evolved stars with wind temperatures below $\simeq 18,000$ K, hydrogen is ionized more readily than in the coronal approximation by the two-stage ionization process, described in Section 5, which lowers the H Ly α peak, but P_{rad} remains double-valued, so that a given input energy may result in more

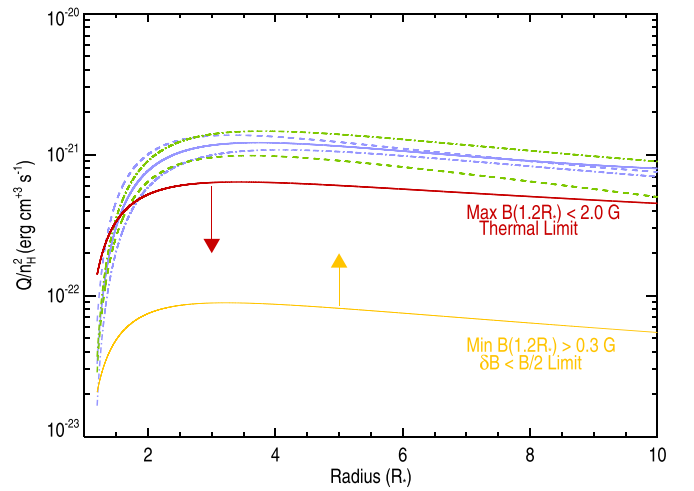


Figure 10. The wind heating rate, Q , derived from Equation (13) divided by the total hydrogen density, $n_H = n_{\text{HI}} + n_{\text{HII}}$, squared. The green and blue lines are computed for a constant temperature of $T_e = 15,400$ K, the temperature estimate based on the UV line analysis. The wind heating increases with increasing magnetic field through the Alfvén wave velocity. The magnetic field constraints are $B > 0.3$ G (gold solid) based on limiting the wave amplitudes to $\delta B/B < 0.5$, and $B < 2.0$ G (red solid) to limit the gas temperature to that observed, i.e., avoiding a coronal wind solution.

than one temperature. In most previous studies, the P_{rad} is artificially adjusted to remove this double-valued nature. In α Boo, the carbon abundance is less than solar, also lowering the power loss. The wind heating increases with increasing magnetic field, i.e., through V_A . To be conservative, we take the lowest 2 G curve in Figure 10 to represent the upper limit to Q/n_H^2 that can lead to temperatures as low as 15,400 K, and hence an upper limit to radial magnetic field. Power loss curves have nonnegligible uncertainties from both the ionization balance computation and electron collision atomic data, which lead to potential uncertainties of $\sim 50\%$.

The actual wind temperature is not only controlled by the local radiative losses, but also by two other factors. Adiabatic cooling of the flow eventually becomes important as the gas density decreases (Hartmann et al. 1982; Falceta-Goncalves et al. 2006), and the energy deposited into the wind also goes into internal energy by ionizing neutral hydrogen and helium. Early studies assumed a constant wind ionization state and neglected the advection term for hydrogen ionization in the energy equation. Including this term makes the differential equations for the thermal structure in Alfvén wave-driven wind modeling particularly stiff. Comparing the advection of the internal energy to the radiative losses (see Goodman & Judge 2012, for details), we find that this term is not significant near the star because hydrogen is already partially ionized at the base of the wind. The wind temperature is sufficiently high to partially ionize Mg II and C II, but the internal energy term may become important at larger radii. For adiabatic cooling to be significant near the star, the flux tubes would have to have very large super-radial expansion factors, which would lead to unrealistic wind acceleration rates.

Lower limits to the magnetic field can be found from the minimum energy required to drive the observed mass-loss rate, and also from the condition that the implied wave magnetic field amplitudes are not too large, i.e., $\delta B_\perp < B/2$. If we take $\sqrt{\langle \delta B_\perp^2 \rangle} = \delta B/2$, then with $v_{\text{turb}} \simeq 0.6 \sqrt{\langle \delta v_\perp^2 \rangle} \simeq 0.6 \sqrt{\langle \delta B_\perp^2 \rangle} / \sqrt{4\pi\rho}$. For $n_H \sim 4 \times 10^7 \text{ cm}^{-3}$, this gives $B_{\text{min}} \simeq 0.5$ G. Taking a more

conservative correspondence between the observed and theoretical turbulent velocities and a lower limit to the mass-loss rate gives an amplitude limit constraint of $B_{\min} > 0.3$ G.

Consideration of the wind heating from the damping of Alfvén waves, and limit on the wave amplitudes provides the semiempirical constraints of the radial magnetic field at $1.2 R_*$ of between 0.3 and 2 G. Considering the series of concatenated assumptions in arriving at these results, it would not be unreasonable to add a factor-of-two uncertainty to these values.

7. Discussion

The HST-STIS line profile analysis, using diagnostics from dominant ionization states combined with the key Si III 1206.5 Å diagnostic, provides a number of interesting new results for α Boo’s outflow for epoch 2018–2019. First we have derived a direct measure of the mean wind temperature at the base of the wind of $\simeq 15,400$ K through the ionization state of Si III, which is tied by charge exchange to the hydrogen ionization balance. The ionization balance in turn provides an estimate of the total mass-loss rate of $2.5 \times 10^{11} M_{\odot} \text{ yr}^{-1}$ and provides predicted centimeter-radio continuum fluxes. An increase of the mass-loss rate to $4.0 \times 10^{11} M_{\odot} \text{ yr}^{-1}$, or an increase in temperature to 18,000 K leads to agreement with the multifrequency VLA data of O’Gorman et al. (2013) for epoch 2011–2012. Comparison of O I epoch 1998, 2018, and 2019, and Mg II epoch 1998 and 2001 mass-loss rates does not reveal any significant changes between these epochs, and these mass-loss rates are significantly lower than most previous estimates.

The first semiempirical mass-loss rate estimates for α Boo ranged from $\dot{M} < 1 \times 10^{-9} \rightarrow 8 \times 10^{-9} M_{\odot} \text{ yr}^{-1}$ at different epochs based on Ca II K line vidicon spectrophotometry and Copernicus moderate-resolution ($R \simeq 43 \text{ km s}^{-1}$) spectra of the Mg II k line (Chiu et al. 1977). Aside from the assumption of a plane-parallel atmosphere and an unrealistic density stratification, another systematic bias resulted from the adoption of low wind microturbulence of 10 km s^{-1} , based on the values from the Ayres & Linsky (1975) model chromosphere. Ayres et al. (1982) estimated $\dot{M} > 3 \times 10^{-10} \rightarrow 2 \times 10^{-9} M_{\odot} \text{ yr}^{-1}$ based on an estimate of the equivalent width of the wind absorption measured from a high-resolution ($R \simeq 11 \text{ km s}^{-1}$) Copernicus Mg II k line profile and assuming $V_{\text{turb}} = 10 \text{ km s}^{-1}$ (McClintock et al. 1978). Clearly the early semiempirical estimates were sensitive to the underlying assumptions in the modeling, and a physically realistic geometry, wind extensions, and high spectral resolution are essential for realistic mass-loss rate estimates. A summary of previous mass-loss rates from empirical estimates, semiempirical and theoretical models, and stellar parameter scalings is given in Table 7. The semitheoretical model of Cranmer & Saar (2011) provides the closest estimate to the mass-loss rates derived here, but we note their mass-loss rate for α Tau is $1.3 \times 10^{-10} M_{\odot} \text{ yr}^{-1}$, which is very different to that derived by Robinson et al. (1998), $1.4 \times 10^{-11} M_{\odot} \text{ yr}^{-1}$.

The closest semiempirical estimate of $2 \times 10^{-10} M_{\odot} \text{ yr}^{-1}$ was derived from partial redistribution profile calculations of the Mg II k line (Drake 1985) matched to IUE spectra (or $1.5 \times 10^{10} M_{\odot} \text{ yr}^{-1}$ when combined with VLA C-band observations; Drake & Linsky 1986b, 1986a). Our work is a development of this approach that uses the synergy of UV spectroscopy and centimeter-radio continuum fluxes, and it is instructive to examine the differences between our works. Drake (1985) solved the radiative transfer problem for the chromosphere+wind as a one-component model and adopted a

spherical wind density stratification but with a small microturbulence of 5 km s^{-1} . Drake (1985) derived two semiempirical atmospheric models, which had maximum wind temperatures of 8000–8450 K, by modeling an IUE high-resolution ($R \simeq 25 \text{ km s}^{-1}$) Mg II k line profile, and they also computed a 6 cm radio continuum flux of ~ 0.4 mJy. This flux compares with the measured VLA value of 0.27 mJy (Drake & Linsky 1986a, 1986b). The main differences between our works are (1) in this work, the line formation and line scattering problems are separated, (2) turbulence and spectral resolution: the high spectral resolution HST-STIS ($R \simeq 3 \text{ km s}^{-1}$) spectra resolve the turbulent velocities of multiple diagnostics revealing higher turbulent velocities, (3) wind temperature: the comparison of Si III 1206.5 Å with other diagnostics provides direct wind temperature estimates that are higher, and (4) comprehensive radio data: the frequency sweep of high S/N VLA radio fluxes includes the L and S bands, which are most sensitive to the wind ionization. Our higher wind temperature and slightly higher hydrogen ionization fractions partially compensate for the lower wind density in our study, noting that our nominal 2018–2019 wind model underestimates the 2011–2012 radio fluxes. We note that the shape of the IUE Mg II k line (from a coaddition of NEWSIPS LWR15997, LWR15998, and LWR15999) is different to that of the HST profiles. Importantly, both our and Drake’s \dot{M} values are much smaller than those predicted by the classic Reimers’ formula, which is weighted to more massive and later spectra-type stars, and α Boo’s mass-loss rate is more in line with $\dot{M} \simeq 1\text{--}3 \times 10^{-11} M_{\odot} \text{ yr}^{-1}$ derived for α Tau (K5 III; Robinson et al. 1998; Wood et al. 2016).

Theoretical wind models have also been used to estimate mass-loss rates from stars with stellar parameters similar to α Boo. Hartmann & MacGregor (1980, Table 3) computed constant damping length WKB Alfvén wave-driven isothermal wind for a surface magnetic field of 10 G and a hydrogen density of 10^{11} cm^{-3} : Models 17 (5000 K) and 18 (10,000 K). These predicted reasonable terminal wind speeds and mass-loss rates of 1.5×10^{-9} and $6.7 \times 10^{-10} M_{\odot} \text{ yr}^{-1}$, respectively. Our lower values for the magnetic field are a result of the lower wind densities and the low observed temperature, i.e., a noncoronal wind. Also the semiempirical damping lengths derived reveal that a spectrum of waves is required, and each period must have its own damping rate to produce the observed wind acceleration. It would be interesting to see if an analytic model could be developed using this information since the wind properties of single red giants appear similar. Cuntz (1990) computed both short- and long-period acoustic wave models for α Boo. Short-period acoustic waves cannot drive reasonable mass-loss rates, but for long-period adiabatic waves with periods of 5.6×10^5 s and 7.0×10^5 s, outflows occurred with mass-loss rates of 4.0×10^{-11} and $1.8 \times 10^{-11} M_{\odot} \text{ yr}^{-1}$ with outflow speeds of 34–38 km s^{-1} , respectively. However, the assumption of adiabatic waves in that work is known to greatly overestimate mass-loss rates in Mira-like variables (Wood 1979), and those results are also extremely sensitive to the wave periods. Previous theoretical investigations of α Boo’s wind have focused on the higher range of mass-loss rates (Haisch et al. 1980; Krogulec 1988), and it would be instructive for future re-investigation of this parameter space.

The β -power-law wind acceleration and terminal velocities derived from the HST-STIS analysis are all similar for the different lines, within the uncertainties, suggesting that the

Table 7
Empirical and Theoretical Mass-loss Rates for Arcturus

Source	Mass-loss Rate ($M_{\odot} \text{ yr}^{-1}$)	Comments
Reimers (1977)	7×10^{-10}	Stellar parameter scaling Equation (1) ($\eta = 0.4$)
Chiu et al. (1977)	$< 8 \times 10^{-9} - 8 \times 10^{-9}$	Semiempirical: $R \simeq 43 \text{ km s}^{-1}$
Copernicus Ca II K, Mg II k		
Hartmann & MacGregor (1980)	$1.5 \times 10^{-9}, 6.7 \times 10^{-10}$	Theoretical: Models 17 and 18, respectively
Ayres et al. (1982)	$> 3 \times 10^{-10} - 2 \times 10^{-9}$	Empirical: $R \simeq 11 \text{ km s}^{-1}$ Copernicus Mg II k
Drake (1985)	2×10^{-10}	Semiempirical: Mg II k
Drake & Linsky (1986b)	$\sim 1.4 \times 10^{-10}$	As above with Ionization from centimeter-radio fluxes
Schröder & Cuntz (2007)	4.2×10^{-10}	Stellar parameter scaling
Cranmer & Saar (2011)	4.7×10^{-11}	Semitheoretical
This Work	$2.5 - 4.0 \times 10^{-11}$	Semiempirical: Mg II , O I, C II, Si III

Note. “Empirical” and “semiempirical” in the third column indicate mass-loss rates based on spectra/fluxes from α Boo.

ETLA approximation for the O I and C II diagnostics was reasonable, especially since the β -power law is not known a priori to be an accurate representation of the outflow. The values of $\beta \sim 1.5$ found here are larger than those derived for later spectra-type red giants using the SEI approximation: α Tau (K5 III) ($\beta = 0.6$; Robinson et al. 1998), μ Gem (M3 III), and γ Cru (M3.4 III) ($\beta = 0.6-0.7$; Rau et al. 2018). It is not known at this time whether this is a result of the SEI approximation adopted in these studies. Nevertheless, these values of β are still much smaller than those derived for the acceleration regions for the intermediate-mass ζ Aur binary systems, i.e., $\beta = 3.5$ (Baade et al. 1996). This difference may be a result of the eccentric binary orbits and/or the entangling of the wind’s magnetic field by an orbit-induced spiral structure (Harper et al. 2005).

Here we have derived the first measures of the radial distribution of turbulence in the outflow acceleration region of a single red giant. The values at $1.2 R_{*}$ are $18-25 \text{ km s}^{-1}$, similar to the SEI results, where the turbulence is assumed constant, with 24 km s^{-1} derived for α Tau (Robinson et al. 1998), and greater than the M spectral-types: 9 km s^{-1} (μ Gem) and 14 km s^{-1} (γ Cru) (Rau et al. 2018). Relaxing the assumption of constant wind turbulence hints that the α -power-law representation adopted here itself may not be sufficient. There is a difference in α -power laws for different diagnostics. The inner constant O I turbulence contrasts with the decline, $V_{\text{turb}} \propto r^{-0.4}$, derived from diagnostics formed farther out. In combination with the trends suggested by the run of turbulence-derived momentum Equation (10) and shown in Figure 8, there may be an initial rise peaking near $1.75 R_{*}$ and then a subsequent decline outwards. Unfortunately the available analytic radial trends in turbulence, i.e., large radii super-Alfvénic, $M_A \gg 1$, flow for high-frequency undamped WKB Alfvén wave-driven winds: $\sqrt{\langle v_{\perp}^2 \rangle} \propto r^{-0.5}$, and for very low-frequency non-WKB waves: $\sqrt{\langle u^2 \rangle} \propto r^{-1}$ (MacGregor & Charbonneau 1994; Charbonneau & MacGregor 1995), are not directly comparable to the present results.

7.1. Implications for the Alfvén Wave Spectrum

The most important result of the Alfvén wave analysis is that the implied wave damping lengths increase with increasing radius as shown in Figure 9. This confirms the trends previously found by Kuin & Ahmad (1989) for the intermediate-mass ζ Aur systems. For a monochromatic frequency, the ion-neutral damping length should decrease with decreasing

ion and neutral particle densities. The wave periods required to match the observed damping rates are annotated in Figure 9 and correspond to hours to days. The longer periods approach the ~ 5 day limit required for a steady wind description, once violated time-dependent treatments are necessary (e.g., Airapetian et al. 2010; Yasuda et al. 2019).

One could envision a spectrum of Alfvén waves with each frequency damping increasingly rapidly (smaller L) with increasing radius. The shorter periods would damp close to the star, with the remaining power spectrum shifting to longer periods. Waves at lower frequencies/longer periods with larger damping lengths then contribute more to the wave energy density at greater radii.

One of the major unknowns in the theory and modeling of magnetic wave-driven winds is the wave energy spectrum originating near the upper chromosphere. A potential excitation mechanism for Alfvén waves is the agitation and twisting of magnetic fields by photospheric granulation where the field lines are tied to gas motions, and the characteristic timescale is the granule convective turn-over time, τ_{gran} . Conservation of mass in the convecting granules gives a robust estimate for the typical granule diameter, $d \sim 10 H_p$, where H_p is the gas pressure scale height (see Magic et al. 2013, and references therein). The characteristic velocity is of the sound speed, c_s , and the timescale is $\tau_{\text{gran}} \sim d/c_s$. Freytag et al. (2002) provided a numerical scaling relation giving the size of granulation cell for given stellar parameters. Airapetian et al. (2000, 2010) and Suzuki (2007) adopted this timescale for the driving frequency or power spectrum of waves in their MHD simulations of evolved cool star winds. For α Boo, $\tau_{\text{gran}} \sim 1$ day, which is consistent with the photospheric granulation noise timescale determined from high-precision SMEI observations of $\tau_{\text{gran}} \simeq 0.50 \pm 0.05$ day (Tarrant et al. 2007).

The wave power spectrum at the base of the wind at $1.2 R_{*}$ is even less well determined because the photospheric power spectrum will have been filtered and augmented by processes in the magnetic chromosphere, e.g., magnetic reconnection (Cranmer 2018), mode convergence in expanding flux tubes, and possibly by parametric decay instability (Réville et al. 2018).

Another condition of the use of the WKB approximation to derive Equations (9) and (11) is that the wavelengths are small compared to the scale height for the Alfvén wave speed, i.e., the wave frequency emanating from the chromosphere is greater than the local critical angular frequency for wave reflection, $\omega_{\text{crit}} = dV_A/dr$, or equivalently, the wave period is less than the critical period, $P_{\text{crit}} = 2\pi/\omega_{\text{crit}}$. These periods for

the α Boo wind model are shown in Figure 9 (right axis) as dashed lines. The critical periods rise very rapidly above the stellar surface until $R \sim 1.7 R_*$, and then drop rapidly again. Waves with periods smaller than these can propagate freely, but periods longer will be partially reflected back down toward the star (An et al. 1990; Barkhudarov 1991; Lou & Rosner 1994; Charbonneau & MacGregor 1995). The lower magnetic field permits longer-period waves to penetrate into the inner wind acceleration region, and periods of 1 day are viable wave periods for ion-neutral damping. Note that long-period waves can still penetrate the wave reflection region (An et al. 1990; Lou & Rosner 1994; Airapetian et al. 2000). For non-WKB-dominated wave-driven winds, the momentum and energy equations adopted here need to be modified, and the presence of wave reflection would also lead to the development of MHD turbulence. Both of these effects would lead to a spatially variable correspondence between V_{turb} and $\sqrt{\langle \delta v_{\perp}^2 \rangle}$. Numerical simulations are required to examine the magnitude of such changes.

7.2. Future Work

There are several systematic uncertainties that could be addressed in future work: (A) investigate changes in the radial description of the turbulence to mimic a wave-driven wind, (B) modeling each of the C II and O I multiplets with simultaneous solutions for each transition, (C) constrain wind temperature gradients in the acceleration region, which might change the predicted centimeter-radio continuum fluxes, and finally (D), Equations (11), (10), and (13) are valid for super-radially diverging flux tubes, in the thin-flux-tube approximation (Hartmann & MacGregor 1982; Falceta-Goncalves et al. 2006). However, the radiative transfer solutions computed here are for spherical geometry. It would be interesting in future work to examine the effects of ensembles of divergent flux-tube geometries on the line profile solutions.

Ohnaka & Morales Marín (2018) spatially resolved the $2.3 \mu\text{m}$ CO spectrum of α Boo at $R \sim 12,000$ with the AMBER instrument at the Very Large Telescope Interferometer. In addition to photospheric CO, they deduce a thin CO layer near $1.04 R_*$, near the temperature minimum of a classical 1D chromosphere and perhaps related to the photospheric H_2O detected by Ryde et al. (2002). Another more extended, and puzzling, CO region reaching $2.6 R_*$ with 1,800 K is also inferred. The implied column densities at this radius are very high, with a total number of hydrogen nuclei $> 2.5 \times 10^{10} \text{ cm}^{-3}$. Because this gas is cold, with a low ionization, it would be relatively invisible in the centimeter-radio continuum and would not emit UV emission lines. However, this cold material would scatter the UV resonance line photons emitted from below, and therefore it must have a small filling factor to be unobserved. The presence of cold dense gas at such large radii requires further confirmation and characterization.

8. Conclusions

The new constraints on the wind properties of α Boo derived from the HST-STIS analysis of Si III 1206.5 Å, O I 1304 Å and O I 1306 Å, C II 1334 Å and C II 1335 Å, and Mg II h 2802 Å profiles show that Si III is a minority species, indicating wind temperatures in the range $T_{\text{wind}} = 15,400\text{--}18,000$ K, and mass-loss rates in the range $\simeq 2.5\text{--}4.0 \times 10^{-11} M_{\odot} \text{ yr}^{-1}$. The latter are significantly smaller than previous semiempirical estimates, and the present result should represent an improvement over previous values in the literature.

An analysis of the wind properties in the framework of WKB Alfvén wave-driven winds provides estimates of the wind magnetic field in the range 0.3–2.0 G. The predicted and observed turbulent wind velocities are in surprisingly good agreement. The conditions for ion-neutral wave damping within the wind show that a spectrum of Alfvén waves with periods of hours to days is required to drive such a wind, a timescale consistent with the photospheric granulation. If an Alfvén wave spectrum is important for mass loss from the noncoronal red giants, then granulation timescales and surface magnetic fields will play an important role in determining the mass-loss rates as a function of stellar parameters. An understanding of the solar Alfvén wave spectrum will likely guide future stellar work. It is likely that non-WKB effects will become important at some radii, and also the concept of a steady wind might break down as the periods become comparable to the wind crossing timescale.

Future high spatial resolution observations with the next-generation VLA and ALMA will further constrain the wind ionization balance and inner-radius boundary radius by establishing the chromospheric extent and the degree of axial symmetry. The symbiotic power of UV spectroscopy and radio diagnostics (Harper 2018) will be greatly enhanced with spatially resolved radio maps of α Boo and other nearby red giants.

Support for programs HST-GO-15234.001-A, HST-AR-14566.001-A, and HST-GO-15904.002-A was provided by NASA through grants from the Space Telescope Science Institute, which is operated by the Associations of Universities for Research in Astronomy, Incorporated, under NASA contract NAS5-26555. Support was also provided by grant No. 80NSSC21K0113 issued by NASA Goddard Space Flight Center to the Center for Astrophysics and Space Astronomy, CU Boulder.

This research has made extensive use of NASA’s Astrophysics Data System, which is operated by the Smithsonian Astrophysical Observatory under NASA Cooperative Agreement 80NSSC21M0056, and the SIMBAD and VizieR databases operated at CDS, Strasbourg, France (Wenger et al. 2000). The NIST Atomic Spectra Database (Kramida et al. 2018) has also proved an invaluable research tool. We have used D. Fanning’s Coyote IDL routines, with thanks.

Facilities: HST, VLA, IUE.

Software: Interactive Data Language (IDL) V8.7 (Exelis Visual Information Solutions, Boulder, Colorado).

Appendix

The radiation dilution factor given in Equation (5) for the case where the surface specific intensity is given by

$$I(\mu) = I(1)\mu,$$

which can be written



$$W_{\text{LD}}(z) = \frac{1}{2} \int_0^{\theta_*} \sin \theta \sqrt{1 - a \sin^2 \theta} d\theta, \quad (\text{A1})$$

where $z = R/R_*$, $a = z^2$, and $\theta_* = \sin^{-1}(1/z)$. This can be evaluated, namely,⁹

⁹ e.g., Wolfram/Alpha.

$$W_{LD}(z) = \frac{1}{8} \left| \frac{2(a-1) \ln[\sqrt{2a} \cos \theta + \sqrt{a \cos 2\theta - a + 2}]}{\sqrt{a}} - \cos \theta \sqrt{2a \cos 2\theta - 2a + 4} \right|_0^{\theta_0}. \quad (\text{A2})$$

ORCID iDs

Graham M. Harper  <https://orcid.org/0000-0002-7042-4541>
 Thomas R. Ayres  <https://orcid.org/0000-0002-1242-5124>

References

- Abia, C., Palmerini, S., Busso, M., & Cristallo, S. 2012, *A&A*, **548**, A55
 Airapetian, V., Carpenter, K. G., & Ofman, L. 2010, *ApJ*, **723**, 1210
 Airapetian, V. S., Ofman, L., Robinson, R. D., Carpenter, K., & Davila, J. 2000, *ApJ*, **528**, 965
 An, C. H., Suess, S. T., Moore, R. L., & Musielak, Z. E. 1990, *ApJ*, **350**, 309
 Andreev, V. E., Efimov, A. I., Samoznaev, L. N., Chashei, I. V., & Bird, M. K. 1997, *SoPh*, **176**, 387
 Arnaud, M., & Rothenflug, R. 1985, *A&AS*, **60**, 425
 Athay, R. G., & Zirker, J. B. 1962, *ApJ*, **136**, 242
 Aurière, M., Konstantinova-Antova, R., Charbonnel, C., et al. 2015, *A&A*, **574**, A90
 Ayres, T. R. 2010, *ApJS*, **187**, 149
 Ayres, T. R. 2018, *AJ*, **156**, 163
 Ayres, T. R., Brown, A., & Harper, G. M. 2003, *ApJ*, **598**, 610
 Ayres, T. R., & Linsky, J. L. 1975, *ApJ*, **200**, 660
 Ayres, T. R., Simon, T., & Linsky, J. L. 1982, *ApJ*, **263**, 791
 Baade, R., Kirsch, T., Reimers, D., et al. 1996, *ApJ*, **466**, 979
 Baliunas, S. L., & Butler, S. E. 1980, *ApJL*, **235**, L45
 Barkhudarov, M. R. 1991, *SoPh*, **135**, 131
 Beckers, J. M. 1976, *ApJ*, **203**, 739
 Belcher, J. W., & Davis, L. J. 1971, *JGR*, **76**, 3534
 Berio, P., Merle, T., Thévenin, F., et al. 2011, *A&A*, **535**, A59
 Bernat, A. P. 1977, *ApJ*, **213**, 756
 Böger, R., Baade, R., Hegmann, M., & Reimers, D. 2003, in *The Future of Cool-Star Astrophysics: 12th Cambridge Workshop on Cool Stars, Stellar Systems, and the Sun*, ed. A. Brown, G. M. Harper, & T. R. Ayres (Boulder, CO: Univ. Colorado), 1058
 Bretherton, F. P., & Garrett, C. J. R. 1968, *RSPSA*, **302**, 529
 Brown, K. I. T., Gray, D. F., & Baliunas, S. L. 2008, *ApJ*, **679**, 1531
 Burnashev, V. I. 1985, *AbaOB*, **59**, 83
 Canfield, R. C., & Ricchiazzi, P. J. 1980, *ApJ*, **239**, 1036
 Carlsson, M., & Judge, P. G. 1993, *ApJ*, **402**, 344
 Carney, B. W., Gray, D. F., Yong, D., et al. 2008, *AJ*, **135**, 892
 Carpenter, J., Iono, D., Kemper, F., & Wootten, A. 2020, arXiv:2001.11076
 Carpenter, K. G., Nielsen, K. E., Kober, G. V., et al. 2018, *ApJ*, **869**, 157
 Carpenter, K. G., Robinson, R. D., Harper, G. M., et al. 1999, *ApJ*, **521**, 382
 Charbonneau, P., & MacGregor, K. B. 1995, *ApJ*, **454**, 901
 Chiu, H. Y., Adams, P. J., Linsky, J. L., et al. 1977, *ApJ*, **211**, 453
 Claret, A., & Bloemen, S. 2011, *A&A*, **529**, A75
 Clarke, N. J., Stancil, P. C., Zygelman, B., & Cooper, D. L. 1998, *JPhB*, **31**, 533
 Cranmer, S. R. 2018, *ApJ*, **862**, 6
 Cranmer, S. R., & Saar, S. H. 2011, *ApJ*, **741**, 54
 Cuntz, M. 1990, *ApJ*, **353**, 255
 Deutsch, A. J. 1956, *ApJ*, **123**, 210
 Drake, S. A. 1985, in *Progress in Stellar Spectral Line Formation Theory*, Proc. Advanced Research Workshop, NATO ASI Series C, ed. J. E. Beckman & L. Crivellari, Vol. 152 (Dordrecht: Reidel), 351
 Drake, S. A., & Linsky, J. L. 1983, *ApJ*, **273**, 299
 Drake, S. A., & Linsky, J. L. 1986a, *IrAJ*, **17**, 288
 Drake, S. A., & Linsky, J. L. 1986b, *AJ*, **91**, 602
 Falcaeta-Gonçalves, D., Vidotto, A. A., & Jatenco-Pereira, V. 2006, *MNRAS*, **368**, 1145
 Field, G. B., & Steigman, G. 1971, *ApJ*, **166**, 59
 Freytag, B., Steffen, M., & Dorch, B. 2002, *AN*, **323**, 213
 Glassgold, A. E., & Huggins, P. J. 1986, *ApJ*, **306**, 605
 Glassgold, A. E., Krstić, P. S., & Schultz, D. R. 2005, *ApJ*, **621**, 808
 Goodman, M. L., & Judge, P. G. 2012, *ApJ*, **751**, 75
 Gunár, S., Koza, J., Schwartz, P., Heinzel, P., & Liu, W. 2021, *ApJS*, **255**, 16
 Hagen, W. 1978, *ApJS*, **38**, 1
 Haisch, B., Schmitt, J. H. M. M., & Rosso, C. 1991, *ApJL*, **383**, L15
 Haisch, B. M., Linsky, J. L., & Basri, G. S. 1980, *ApJ*, **235**, 519
 Haisch, B. M., Linsky, J. L., Weinstein, A., & Shine, R. A. 1977, *ApJ*, **214**, 785
 Harper, G. M. 1994, *MNRAS*, **268**, 894
 Harper, G. M. 2001, in *ASP Conf. Ser.*, 223, 11th Cambridge Workshop on Cool Stars, Stellar Systems and the Sun, ed. R. J. Garcia Lopez, R. Rebolo, & M. R. Zapaterio Osorio (San Francisco, CA: ASP), 368
 Harper, G. M. 2018, in *ASP Conf. Ser.*, 517, Science with a Next Generation Very Large Array, ed. E. Murphy (San Francisco, CA: ASP), 265
 Harper, G. M., Brown, A., Ayres, T., & Sim, S. A. 2004, in *IAU Symp.* 219, Stars as Suns: Activity, Evolution and Planets, ed. A. K. Dupree & A. O. Benz (San Francisco, CA: ASP), 651
 Harper, G. M., Brown, A., Bennett, P. D., et al. 2005, *AJ*, **129**, 1018
 Harper, G. M., O’Riain, N., & Ayres, T. R. 2013, *MNRAS*, **428**, 2064
 Harper, G. M., Wood, B. E., Linsky, J. L., et al. 1995, *ApJ*, **452**, 407
 Hartmann, L., Avrett, E., & Edwards, S. 1982, *ApJ*, **261**, 279
 Hartmann, L., & Avrett, E. H. 1984, *ApJ*, **284**, 238
 Hartmann, L., & MacGregor, K. B. 1980, *ApJ*, **242**, 260
 Hartmann, L., & MacGregor, K. B. 1982, *ApJ*, **257**, 264
 Heiter, U., Jofré, P., Gustafsson, B., et al. 2015, *A&A*, **582**, A49
 Henry, G. W., Fekel, F. C., Henry, S. M., & Hall, D. S. 2000, *ApJS*, **130**, 201
 Höfner, S., & Olofsson, H. 2018, *A&ARv*, **26**, 1
 Hollweg, J. V. 1971, *JGR*, **76**, 5155
 Holzer, T. E., Fla, T., & Leer, E. 1983, *ApJ*, **275**, 808
 Holzer, T. E., & MacGregor, K. B. 1985, in *Mass Loss from Red Giants*, ed. M. Morris & B. Zuckerman, Vol. 117 (Dordrecht: Reidel), 225
 Hummer, D. G. 1988, *ApJ*, **327**, 477
 Jacques, S. A. 1977, *ApJ*, **215**, 942
 Jofré, P., Heiter, U., Soubiran, C., et al. 2014, *A&A*, **564**, A133
 Jofré, P., Heiter, U., Soubiran, C., et al. 2015, *A&A*, **582**, A81
 Jordan, C. 1986, *IrAJ*, **17**, 227
 Jordan, C., Mendoza, B., & Gill, R. S. 1984, in *The Hydromagnetics of the Sun*, Proc. 4th European Meeting on Solar Physics, ESA-SP220, ed. T. D. Guyenne & J. J. Hunt, 133
 Judge, P. G. 1986, *MNRAS*, **221**, 119
 Judge, P. G. 1992, in *ASP Conf. Ser.* 26, Cool Stars, Stellar Systems, and the Sun, ed. M. S. Giampapa & J. A. Bookbinder (San Francisco, CA: ASP), 403
 Judge, P. G., & Jordan, C. 1991, *ApJS*, **77**, 75
 Judge, P. G., & Stencel, R. E. 1991, *ApJ*, **371**, 357
 Keenan, P. C., & McNeil, R. C. 1989, *ApJS*, **71**, 245
 Kramida, A., Yu. Ralchenko, R. J., & NIST ASD Team 2018, NIST Atomic Spectra Database, v.5.6.1, <https://physics.nist.gov/asd>
 Krogulec, M. 1988, *AcA*, **38**, 107
 Kudritzki, R. P., & Reimers, D. 1978, *A&A*, **70**, 227
 Kuin, N. P. M., & Ahmad, I. A. 1989, *ApJ*, **344**, 856
 Lacour, S., Meimon, S., Thiébaud, E., et al. 2008, *A&A*, **485**, 561
 Lamers, H. J. G. L. M., & Cassinelli, J. P. 1999, *Introduction to Stellar Winds* (Cambridge: Cambridge Univ. Press)
 Landi, E., & Landini, M. 1999, *A&A*, **347**, 401
 Linsky, J. L., & Haisch, B. M. 1979, *ApJL*, **229**, L27
 Lou, Y.-Q., & Rosner, R. 1994, *ApJ*, **424**, 429
 MacGregor, K. B., & Charbonneau, P. 1994, *ApJ*, **430**, 387
 Maeckle, R., Holweger, H., Griffin, R., & Griffin, R. 1975, *A&A*, **38**, 239
 Magic, Z., Collet, R., Asplund, M., et al. 2013, *A&A*, **557**, A26
 Mallik, S. V. 1982, *JApA*, **3**, 39
 Mallik, S. V. 1993, *ApJ*, **402**, 303
 McClintock, W., Moos, H. W., Henry, R. C., Linsky, J. L., & Barker, E. S. 1978, *ApJS*, **37**, 223
 McMurry, A. D. 1999, *MNRAS*, **302**, 37
 Monteiro, T. S., Danby, G., Cooper, I. L., Dickinson, A. S., & Lewis, E. L. 1988, *JPhB*, **21**, 4165
 Murphy, E. J., Bolatto, A., Chatterjee, S., et al. 2018, in *ASP Conf. Ser.*, 517, Science with a Next Generation Very Large Array, ed. E. Murphy (San Francisco, CA: ASP), 3

- O’Gorman, E., & Harper, G. M. 2011, in ASP Conf. Ser., 448, 16th Cambridge Workshop on Cool Stars, Stellar Systems, and the Sun, ed. C. Johns-Krull, M. K. Browning, & A. A. West (San Francisco, CA: ASP), 691
- O’Gorman, E., Harper, G. M., Brown, A., Drake, S., & Richards, A. M. S. 2013, *AJ*, 146, 98
- Ohnaka, K., & Morales Marín, C. A. L. 2018, *A&A*, 620, A23
- Olson, G. L., Auer, L. H., & Buchler, J. R. 1986, *JQSRT*, 35, 431
- Oster, L., & Ulmschneider, P. 1973, *A&A*, 29, 1
- Petretti, C. G., Akiyama, K., & Matthews, L. D. 2021, arXiv:2110.01625
- Piddington, J. H. 1956, *MNRAS*, 116, 314
- Rau, G., Nielsen, K. E., Carpenter, K. G., & Airapetian, V. 2018, *ApJ*, 869, 1
- Redfield, S., & Linsky, J. L. 2002, *ApJS*, 139, 439
- Redfield, S., & Linsky, J. L. 2004, *ApJ*, 602, 776
- Redfield, S., & Linsky, J. L. 2008, *ApJ*, 673, 283
- Reimers, D. 1975a, *MSRSL*, 8, 369
- Reimers, D. 1975b, in Problems in Stellar Atmospheres and Envelopes, ed. B. Baschek, W. H. Kegel, & G. Traving (New York: Springer), 229
- Reimers, D. 1977, *A&A*, 61, 217
- Reimers, D. 1987, in IAU Symp. 122, Circumstellar Matter, ed. I. Appenzeller & C. Jordan (Dordrecht: Reidel), 307
- Renzini, A. 1977, in Saas-Fee Advanced Course 7: Advanced Stages in Stellar Evolution, ed. P. Bouvier & A. Maeder (Sauverny: Observatoire de Genève), 151
- Réville, V., Tenerani, A., & Velli, M. 2018, *ApJ*, 866, 38
- Robinson, R. D., Carpenter, K. G., & Brown, A. 1998, *ApJ*, 503, 396
- Ryde, N., Lambert, D. L., Richter, M. J., & Lacy, J. H. 2002, *ApJ*, 580, 447
- Ryde, N., Gustafsson, B., Edvardsson, B., et al. 2010, *A&A*, 509, A20
- Sanner, F. 1976, *ApJS*, 32, 115
- Sasselov, D. D., & Lester, J. B. 1994, *ApJ*, 423, 785
- Schoenberg, K. 1985, *A&A*, 148, 405
- Scholz, T. T., & Walters, H. R. J. 1991, *ApJ*, 380, 302
- Schröder, K. P., & Cuntz, M. 2005, *ApJL*, 630, L73
- Schröder, K. P., & Cuntz, M. 2007, *A&A*, 465, 593
- Sennhauser, C., & Berdyugina, S. V. 2011, *A&A*, 529, A100
- Sigut, T. A. A., & Pradhan, A. K. 1995, *JPhB*, 28, 4879
- Smith, S. J., Chutjian, A., Mawhorter, R. J., Williams, I. D., & Shemansky, D. E. 1993, *JGR*, 98, 5499
- Smith, V. V., Cunha, K., Shetrone, M. D., et al. 2013, *ApJ*, 765, 16
- Stancil, P. C., Schultz, D. R., Kimura, M., et al. 1999, *A&AS*, 140, 225
- Suzuki, T. K. 2007, *ApJ*, 659, 1592
- Tarrant, N. J., Chaplin, W. J., Elsworth, Y., Spreckley, S. A., & Stevens, I. R. 2007, *MNRAS*, 382, L48
- van Leeuwen, F. 2007, Hipparcos, the New Reduction of the Raw Data, Vol. 350 (Berlin: Springer)
- Wenger, M., Ochsenbein, F., Egret, D., et al. 2000, *A&AS*, 143, 9
- Weymann, R. 1962, *ApJ*, 136, 844
- Wilson, O. C. 1960, *ApJ*, 132, 136
- Wood, B. E., Müller, H.-R., & Harper, G. M. 2016, *ApJ*, 829, 74
- Wood, P. R. 1979, *ApJ*, 227, 220
- Worrall, G., & Wilson, A. M. 1973, *VA*, 15, 39
- Yasuda, Y., Suzuki, T. K., & Kozasa, T. 2019, *ApJ*, 879, 77
- Zuckerman, B., Kim, S. S., & Liu, T. 1995, *ApJL*, 446, L79